doi:10.26443/seismica.v5i1.1842

SEISMICA

Modeling fluid-driven fault slip dynamics with shear-induced dilation and compaction

Betti Hegyi *[1], **Luca Dal Zilio** [2,3], **Whitney Behr** [1], **Taras Gerya** [4]

[1]Structural Geology and Tectonics Group, Geological Institute, Department of Earth and Planetary Sciences, ETH Zurich, Sonneggstrasse 5, 8092 Zurich, Switzerland, [2]Earth Observatory of Singapore, Nanyang Technological University, Singapore, [3]Asian School of the Environment, Nanyang Technological University, Singapore, [4]Geophysical Fluid Dynamics Group, Institute of Geophysics, Department of Earth and Planetary Sciences, ETH Zurich, Sonneggstrasse 5, 8092 Zurich, Switzerland

Author contributions: *Conceptualization*: All authors. *Methodology*: Betti Hegyi, Luca Dal Zilio, Taras Gerya. *Software*: Luca Dal Zilio, Taras Gerya. *Investigation*: Betti Hegyi. *Writing - Original draft*: Betti Hegyi, Whitney Behr, Luca Dal Zilio. *Writing - Review & Editing*: All authors. *Visualization*: Betti Hegyi, Whitney Behr. *Supervision*: Luca Dal Zilio, Whitney Behr, Taras Gerya. *Funding acquisition*: Whitney Behr.

Abstract The role of pore fluid pressure variations in influencing seismic and aseismic fault slip remains a major challenge in earthquake mechanics. In this study, we employ the Hydro-Mechanical Earthquake Cycle (H-MEC) code to simulate fluid-driven earthquake cycles in a fully coupled solid-fluid continuum framework. The code incorporates a non-linear, plastic strain-rate dependent dilatancy-compaction formulation to explore the interplay between shear induced (de)compaction, fluid pressurization, and fault dilation. Our results demonstrate a diverse range of seismic slip behaviors, including fast dynamic rupture, slow slip transients, and stable aseismic creep. During seismic slip events, pore fluid pressurization reduces both fault shear strength and resistance to compaction, facilitating dynamic rupture as a solitary pore pressure wave. We find that fault hydraulic properties, such as porosity and permeability, critically govern slip dynamics by controlling the temporal evolution of fluid pressure transients and effective stress. We also find that shear-induced dilatancy plays a role in the long-term stabilization of the fault, while compressibility has a significant influence on the initial response of the fault, deciding whether the fault hosts seismic or aseismic slip. Our findings emphasize the importance of incorporating realistic hydro-mechanical processes in models, to explore the evolution of fluid pressure, (de)compaction and dilatancy, and their impact on the seismic slip modes.

Production Editor:
Andrea Llenos
Handling Editor:
Pathikrit Bhattacharya
Copy & Layout Editor:
Hannah F. Mark

Signed reviewer(s):
Eric Dunham

Received:
July 11, 2025
Accepted:
May 19, 2026
Published:
June 11, 2026

1 Introduction

The role of fluids in influencing fault slip behaviors is increasingly recognized based on natural observations, models, and experiments. The primary effect of fluids is through the buildup and release of fluid pressure, which strongly influences the hydro-mechanical dynamics of fault slip. Examples include both induced seismicity, such as seismic events triggered by fluid injection into reservoirs (e.g., Ellsworth, 2013; Alghannam and Juanes, 2020), and natural seismic activities, including the triggering of seismic swarms by natural injection of deep fluids into upper crustal fault zones (e.g., Hainzl, 2004; Miller, 2020; Ross et al., 2020). Furthermore, several studies suggest that the presence of fluids may be linked to the initiation of slow-slip events in various geological settings, including strike-slip faults and subduction zones (Bürgmann, 2018; Frank et al., 2015). This in particular indicates that fluid-triggered aseismic slip transients can significantly impact the long-term seismic cycle. Supporting evidence is also found in the rock record, where faults exhumed from the seismogenic zone and the source depths of slow slip and tremor commonly bear signs of fluid circulation, such as veins and metasomatic fronts (e.g., Angiboust et al., 2015; Fagereng et al., 2017; Behr and Bürgmann, 2020; Condit and French, 2022; Muñoz-Montecinos and Behr, 2023; Sibson, 2017). Together, these observations underscore the critical influence of fluids on the hydro-mechanical dynamics of fault slip, setting the stage for a deeper exploration of their role on fault mechanics and earthquake physics.

Over the past several decades, a vast body of work has focused on understanding how the friction coefficient and strength of faults evolve during fault slip. This line of research, grounded in laboratory experiments, has led to the development of a sophisticated framework known as rate- and state-dependent friction (Dieterich, 1978; Ruina, 1983; Marone, 1998; Scholz, 1998). While the variations in friction at slow slip rates (below 1 mm/s) are relatively minor (Dieterich, 1978; Ruina, 1983), at faster rates – akin to those observed in rapid seismic events – these changes become significantly more pronounced due to dynamic weakening processes (e.g., Tsutsumi and Shimamoto, 1997; Rice, 2006; Di Toro et al., 2011; Goldsby and Tullis, 2011; Noda and Lapusta, 2013). Nonetheless, the stress drop observed in most earthquakes falls within the range of 1 to 10 MPa (Abercrombie and Rice, 2005; Allmann and Shearer, 2009), possibly indicating that stress levels on faults are comparatively low before the onset

*Corresponding author: betti.hegyi@eaps.ethz.ch

of rupture (Noda et al., 2009). A plausible explanation for this phenomenon involves elevated pore pressures that reduce the effective normal stress on faults, making them chronically weak and thereby facilitating earthquake nucleation under low shear stress conditions (Rice, 2006; Lambert et al., 2021).

Despite ample evidence affirming the interaction between solids and fluids in fault zones (Miller, 2013, for a review), many earthquake models overlook the variations in fluid pressure that may coincide with fault slip. Commonly, these models presuppose a permanently over-pressured fault to achieve realistic conditions of stress drops and the slip behaviors observed in both regular earthquakes and slow-slip phenomena (e.g., Lapusta et al., 2000; Liu and Rice, 2007; Barbot et al., 2012; Dal Zilio et al., 2020; Behr et al., 2021). Yet, considering that pore-fluid pressure may fluctuate throughout the earthquake cycle, as suggested, for example, by geologic observations from natural fault zones (Sibson, 1992b; Cox, 2005), these variations in fluid pressure could have an important effect on the dynamics of seismic cycles. More recent investigations have explored various dimensions of solid-fluid interactions in fault zones through physics-based numerical models, revealing that fluids could play a pivotal role in aftershocks, transient creep, seismic swarms, and slow-slip occurrences (Miller et al., 2004; Heimisson et al., 2019; Zhu et al., 2020; Petrini et al., 2020; Yang and Dunham, 2021; Dal Zilio et al., 2022; Dal Zilio and Gerya, 2022; Marguin and Simpson, 2023).

When a fluid-filled fault experiences shear, it can lead to shear-induced dilation or compaction, which respectively decrease or increase pore pressure within the fault core. This dynamic clamping or unclamping of the fault affects fault slip, making it crucial to understand these mechanisms for studying earthquake source processes. Theoretical (Rice and Rudnicki, 1979; Segall and Rice, 1995; Segall et al., 2010) and experimental work (Marone, 1998; Brantut, 2020; Proctor et al., 2020; Aben and Brantut, 2021) in the past several decades has explored the process of dilatancy strengthening, which quenches the instability on the fault, by opening additional pore space, decreasing fluid pressure and increasing effective normal stress, thus suppressing slip acceleration. On the other hand, shear induced compaction (Segall and Rice, 1995; Connolly and Podladchikov, 2000; Yarushina et al., 2015) causes plastic collapse of pores, which increases the pore fluid pressure, thus reducing frictional strength and destabilising the fault. These two processes in nature should therefore compete and can counteract each other (Fig. 1), resulting in either net compaction or dilation. To assist an earthquake nucleation in a fluid-filled fault zone, the compaction must exceed dilation, thereby increasing the pore fluid pressure, and decreasing the shear stress such that a shear instability can grow into a dynamic rupture. In recent years, dilation rates have been measured in experimental studies of fault gouges as well as on natural faults (Marone et al., 1990; Lockner and Byerlee, 1994; Samuelson et al., 2009; Beeler et al., 2018; Xing et al., 2019; Brantut, 2020; Aben and Brantut, 2021; Ashman and Faulkner, 2023), providing mostly qualitative evidence of slip stabilization due to dilation. As a result, the currently accepted hydromechanical model for fault slip stability primarily considers only rate-dependent dilatancy (Segall and Rice, 1995). However, recent laboratory experiments utilizing an innovative procedure designed to measure pore pressure and hydromechanical interactions during rupture nucleation and slip (Proctor et al., 2020; Aretusini et al., 2021) have highlighted the importance of both dilatancy and compaction (that is, pore collapse) during nucleation and rapid slip, which together contribute to instability. Consequently, better constraints are needed to fully understand the interplay between these mechanisms and their impact on fault stability.

In this study, we build upon these kinds of experimental observations through the application of the continuum-based Hydro-Mechanical Earthquake Cycle code, H-MEC (Petrini et al., 2020; Dal Zilio et al., 2022), to study fluid-induced seismic and aseismic slip on strike-slip faults. Our focus is on modeling sequences of earthquakes and aseismic slip within a medium that is poro-visco-elasto-plastic and compressible, examining how variations in fluid and fault zone characteristics (such as porosity, permeability, and dilatancy) affect the style and speed of fault slip, as well as the frequency of earthquake occurrences. In the models presented in this paper, fault slip emerges self-consistently from the coupled evolution of solid deformation and fluid pressure evolution.

2 Methodology

The H-MEC code is based on staggered finite differences and marker-in-cell techniques (SFD + MIC) in two dimensions (2-D) and features a fully coupled solid-fluid system (Dal Zilio et al., 2022). H-MEC incorporates fault slip, pore pressure diffusion, fully coupled poroelasticity, and inertial wave-mediated effects. An adaptive time-stepping algorithm allows the correct resolution of both long- and short-time scales, spanning years during slow tectonic loading to milliseconds during the propagation of dynamic ruptures. We apply the methodology in a simple, two-dimensional plane-strain model of a strike-slip fault, building on the previous results from Dal Zilio et al. (2022). The reference parameters are chosen to be representative of natural fault zone properties (Table 1).

2.1 Governing equations

The four governing equations are the total momentum (1), solid mass (2), fluid momentum (3) and fluid mass (4) conservation equations (e.g., Yarushina and Podladchikov, 2015; Gerya, 2019; Petrini et al., 2020):

$$\frac{\partial {\sigma'}^{t}_{ij}}{\partial x_j} - \frac{\partial P^t}{\partial x_i} + \rho^t g_i = \rho^t \frac{D^s v_i^s}{Dt} \quad (1)$$

$$\frac{\partial v_x^s}{\partial x} + \frac{\partial v_y^s}{\partial y} = -\frac{P^t - P^f}{\eta^\phi (1-\phi)} - \frac{1}{K_d}\left(\frac{D^s P^t}{Dt} - \alpha \frac{D^f P^f}{Dt}\right) + 2\dot{\varepsilon}_{II_{(plastic)}} D \quad (2)$$

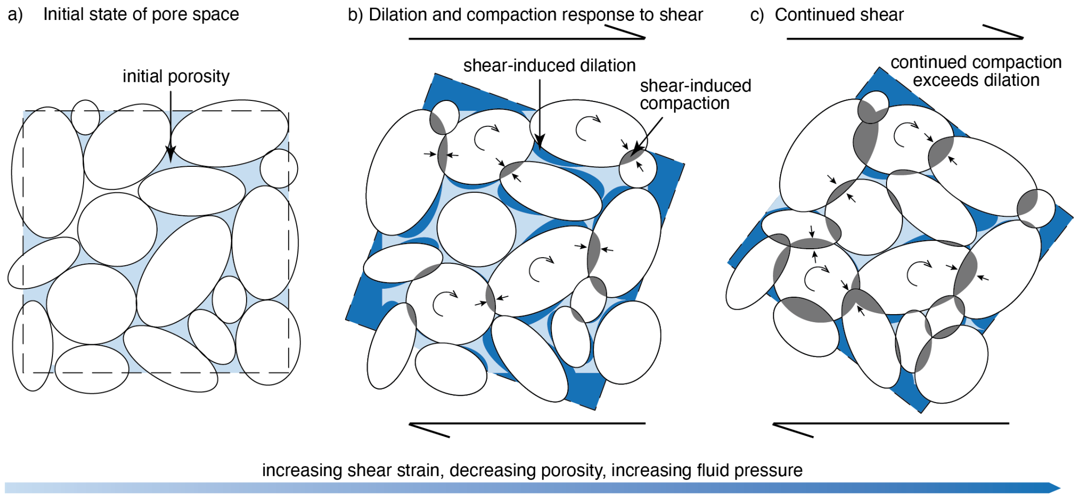

Figure 1 Evolution of pore space during shear induced compaction and dilation. a) Initial state of pore space. b) The shear strain increase activates the response of dilation and compaction, while the porosity decreases, and the fluid pressure increases. c) Compaction exceeds dilation due to the continued shear.

$$v_i^D = -\frac{k}{\eta_f}\left(\frac{\partial P^f}{\partial x_i} - \rho_f g_i + \rho^f \frac{D^s v_i^s}{Dt}\right) \tag{3}$$

$$\frac{\partial v_x^D}{\partial x} + \frac{\partial v_y^D}{\partial y} = \frac{P^t - P^f}{\eta^\phi (1-\phi)} + \frac{\alpha}{K_d}\left(\frac{D^s P^t}{Dt} - \frac{1}{B}\frac{D^f P^f}{Dt}\right) - 2\dot{\varepsilon}_{II_{(plastic)}} D \tag{4}$$

where superscripts s, f, and t stand for solid, fluid matrix, and total properties, respectively; and $\frac{D^s}{Dt}$ and $\frac{D^f}{Dt}$ represent the Lagrangian time derivative in the solid and fluid reference frame, respectively. σ'^t_{ij} is the deviatoric stress for the bulk material, P and ρ are respectively the pressure and density, and g_i is the i-th gravity component. ϕ is the porosity, and v_i^s and v_i^f are the i-th component of the solid and fluid velocities. K_d is the drained bulk modulus, α is the Biot-Willis coefficient, η^ϕ is the effective compaction viscosity, $\dot{\varepsilon}_{II_{(plastic)}}$ is the second invariant of the plastic strain rate, and D is the dilatancy coefficient. v_i^D is the i-th component of Darcy's velocity ($v_i^D = \phi\left(v_i^f - v_i^s\right)$), k is the permeability, η_f is the fluid viscosity and B is the Skempton's coefficient. Equations 1, 2, 3, 4 are solved across the entire model domain (Fig. 3b). The primary solved variables are the solid velocity components (v_x^s, v_y^s), the Darcy fluid velocity components (v_x^D, v_y^D), the total pressure (P^t), and the fluid pressure (P^f).

The Biot-Willis coefficient can be calculated as:

$$\alpha = 1 - \frac{K_d}{K_s}, \tag{5}$$

where K_s is the solid bulk modulus.

The drained bulk modulus K_d is

$$K_d = (1-\phi)\left(\frac{1}{K_\phi} + \frac{1}{K_s}\right)^{-1}, \tag{6}$$

where the effective bulk modulus of pores, K_ϕ is given by:

$$K_\phi = \frac{2m}{(m+1)}\frac{G}{\phi}, \tag{7}$$

where m is a geometrical factor and G is the shear modulus.

The Skempton's coefficient B is calculated as:

$$B = \frac{\frac{1}{K_d} - \frac{1}{K_s}}{\frac{1}{K_d} - \frac{1}{K_s} + \phi\left(\frac{1}{K_f} - \frac{1}{K_s}\right)}, \tag{8}$$

where K_f is the fluid bulk modulus.

The effective visco-plastic compaction viscosity $\left(\eta^\phi\right)$ is expressed as (Yarushina and Podladchikov (2015)):

$$\eta^\phi = \frac{2m}{(m+1)}\frac{\eta_{(plastic)}}{\phi}, \tag{9}$$

where $\eta_{(plastic)}$ is the effective visco-plastic shear viscosity of the solid matrix, and is calculated as

$$\eta_{(plastic)} = \frac{\sigma_{II}}{2\,\dot{\varepsilon}'_{II\,(\text{plastic})}}, \tag{10}$$

where σ_{II} is second invariant of the deviatoric stress tensor, and $\dot{\varepsilon}'_{II\,(\text{plastic})}$ is the square root of the plastic component of the deviatoric strain rate.

This formulation follows Yarushina and Podladchikov (2015). η^ϕ represents an effective resistance to volumetric deformation of a plastically yielding porous material, rather than a fixed bulk material viscosity, and it is determined from the changes in the visco-plastic shear viscosity (shear resistance) of the solid matrix. As plastic yielding initiates and strain rate increases, $\eta_{(plastic)}$ decreases, which leads to a proportional reduction in η^ϕ, and to the promotion of visco-plastic compaction. Therefore, compaction is primarily activated during periods of active deformation, with a direct dependence on slip velocity, which correlates positively with visco-plastic strain rate inside the actively slipping fault. The changes in η^ϕ thus emerge from the coupled decrease in both shear and compaction resistance with increasing slip velocity, reflecting the activation of grain crushing, microcracks, pore collapse or related damage processes during shear. This provides a physical basis for scaling compaction viscosity with visco-plastic shear viscosity. Also, some laboratory experiments (e.g., Proctor et al., 2020; Aretusini et al., 2021) and theoretical studies (e.g., Iverson, 2005; Goren et al., 2010) support shear-induced compaction and rapid shear-induced pressurization, thereby providing support to our simplified scaling model for visco-plastic compaction viscosity, although multiple mechanisms (including thermal pressurization) may contribute to the observed pore fluid pressure evolution in these experiments. In the appendix we provide a plot showing the evolution of the parameter η^{ϕ} through multiple seismic cycles.

A porosity dependent permeability has been implemented:

$$k = k_0 \left(\frac{\phi}{\phi_0}\right)^n, \tag{11}$$

where n is the permeability exponent that can vary significantly (from 1 up to 50) (Yarushina et al., 2013), k_0 is the reference permeability, ϕ_0 is the reference porosity and equals to 1%.

The continuity equations for both solids and fluids, referred to as Eqs. 2 and 4, incorporate terms related to poro-elasticity. This concept accounts for the compressibility of both the solid skeleton and the fluid within it. It also addresses how the interconnected spaces within the porous material can undergo viscous flow and elastic changes in volume, either compacting or expanding. Since these two equations are linked, any change in the volume of the solid framework due to compaction or expansion directly affects, and is affected by, the fluid dynamics. This interaction creates a system where the behavior of the fluid and the solid are interconnected and influence each other, known as a fully coupled hydro-mechanical system (e.g., Yarushina and Podladchikov, 2015; Gerya, 2019; Petrini et al., 2020). Within this framework, fault slip behavior is governed by the following mechanisms: (1) visco-plastic compaction, which represents irreversible deformation controlled by the effective (visco-plastic) compaction viscosity. During yielding, compaction localizes through a decrease in the effective compaction viscosity (η^{ϕ}), driven by a reduction in the visco-plastic shear viscosity ($\eta_{plastic}$), which lowers the resistance of the pore space to volumetric compaction (Eqs. 9 and 10). (2) Poro-elastic (de)compaction, which allows the reversible elastic opening or closure of the pore space in response to pore pressure variations, modulated by the Biot-Willis and Skempton coefficients. (3) Dilatancy corresponds to shear induced creation of pore space during plastic deformation (e.g. by grain rotation), which reduces pore pressure and increases effective normal stress. During transient slip, the poro-elastic component therefore evolves inversely to dilatancy, acting elastically to balance the inelastic pore-space opening.

2.2 Rate-dependent strength of fault

We use a rate-dependent strength formulation to calculate frictional resistance to determine the yield stress during fault slip, in order to understand the complex behaviors of fault slip, including transitions between seismic and aseismic slip. H-MEC employs a visco-elasto-plastic Maxwell rheology, integrated with a rate-dependent Drucker-Prager yielding criterion affected by the effective pressure, which is the difference between the total and fluid pressures in the bulk material (Drucker and Prager, 1952). The power-law formulation for the rate-dependent strength to govern plastic deformation (Yi et al., 2018) is as follows:

$$\sigma'_{II} = \sigma_0 \left(\frac{\dot{\varepsilon}'_{II\,(\mathrm{plastic})}}{\varepsilon_0}\right)^{\gamma} \tag{12}$$

$$\sigma_0 = c + f\left(P^t - P^f\right) \tag{13}$$

where σ'_{II} represents the square root of the second invariant of the deviatoric stress tensor, σ_0 denotes the reference strength determined by the Drucker-Prager yielding criterion, $\dot{\varepsilon}'_{II\,(\mathrm{plastic})}$ is the square root of the plastic component of the deviatoric strain rate, γ is the rate-strengthening exponent, c stands for cohesional strength, f is the friction coefficient, and ε_0 indicates the reference strain rate. The rate-strengthening exponent γ, akin to the direct effect of rate-and-state dependent friction, has substantial laboratory validation but does not rely on evolutionary frictional effects (Yi et al., 2018). Instead, the weakening mechanism of our model is driven by the evolution of pore-fluid pressure (P^f), which is influenced by the shear induced (de)compaction/dilation, as reflected in Eq. 13. The role of the rate-strengthening exponent γ is explored in our simulations, particularly its effect on the model behavior in the seismogenic zone. We present numerical tests of three γ values (Fig. 2). In Fig. 2a, the mean yield stresses show an approximately 2% difference with increasing γ, while the peak maximum slip rate decreases by approximately 40% with increasing γ (Fig. 2a and b). However, the measured slip rates remain within the range observed in natural fault zones. Moreover, the overall model behavior remains unchanged, with the timing of the first four events nearly identical across the three models (Fig. 2c). This suggests that the rate-strengthening exponent γ has minimal influence on the slip mode, or on the convergence of the model evolution, implying that the velocity-weakening effect, driven by pressure changes (and thereby (de)compaction/dilation processes), exerts the main influence on the seismic slip mode. The use of the adopted plasticity model also offers a complement to the frequently utilized rate-and-state dependent friction law for seismic cycle modeling (Ruina, 1983; Lapusta et al., 2000; Chen and Lapusta, 2009; Erickson and Day, 2016; Herrendörfer et al., 2018; van den Ende et al., 2018). For a comprehensive summary of rheology, time-stepping algorithm, and the discretization of governing equations we refer to Dal Zilio et al. (2022).

2.3 Treatment of Dilatancy

The dilatancy coefficient in Eqs. 2 and 4 represents the volumetric expansion associated with shear deforma-

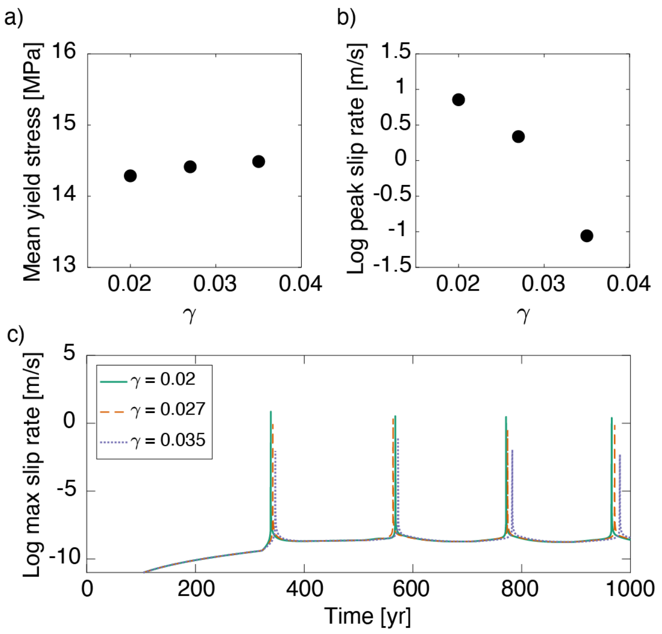

Figure 2 Results of γ tests at three different values: γ = 0.02 0.027, 0.035 tests. a) Mean yield stresses during the first events. b) Peak maximum slip rates during the first events. c) Evolution of the slip rate throughout five events in three different models.

tion, a process that can reduce pore pressure. Experimental studies show that dilatancy varies with strain, increasing toward a peak value and diminishing thereafter (e.g., Brace et al., 1966; Zhao and Cai, 2010). Furthermore, the dilatancy also increases with confining stress (Zhao and Cai, 2010). To simplify our models, we assume a constant dilatancy coefficient, which captures the maximum stabilizing effect of dilatancy without accounting for its specific evolution over time or strain. The dilatancy model here depends solely on plastic strain rate, and therefore scales with slip velocity. To systematically explore the role of dilatancy, we adopt a stepwise approach with increasing complexity.

Step 1: Analytical Derivation. First, we derive a simplified analytical expression for critical dilatancy to identify the general conditions under which dilatancy dominates over visco-plastic compaction for the case of steady-state pressure and constant pore volume. This derivation assumes zero compressibility with $\frac{1}{K_s} = \frac{1}{K_f} = \beta_s = \beta_f = 0$ and therefore $\alpha = B = 1$, and we use a low permeability ($k_0 = 10^{-20}\ m^2$) to ensure negligible fluid pressure diffusion. The critical dilatancy (D^{cr}), defined as the condition under which dilatancy-related pore volume increase exactly compensates the volumetric effect of plastic compaction, is then derived as follows:

$$\frac{P^t - P^f}{\eta^{\phi}(1-\phi)} = 2\,\dot{\varepsilon}'_{II\ (\text{plastic})}\ D^{cr} \tag{14}$$

where η^{ϕ} represents the effective compaction viscosity from Eq. 9.

Substituting the expression for $\eta_{\ (\text{plastic})}$ (Eq. 10) into η^{ϕ}, and assuming $\sigma_{II} = \sigma_{yield}$:

$$\eta^{\phi} = \frac{2m}{(m+1)\phi}\,\frac{\sigma_{yield}}{2\,\dot{\varepsilon}'_{II\ (\text{plastic})}}. \tag{15}$$

Neglecting effects of rate-dependence for the material strength (i.e., assuming $\gamma = 0$) and using the simplified rate-independent Drucker-Prager yield criterion, where $\sigma_{yield} = \sigma_0 = c + f(P^t - P^f)$, we can express the pressure difference as:

$$P^t - P^f = \frac{\sigma_{yield} - c}{f}. \tag{16}$$

This allows us to rewrite the initial equation as:

$$\frac{P^t - P^f}{\eta^{\phi}(1-\phi)} = \frac{(\sigma_{yield} - c)\ (m+1)\ 2\dot{\varepsilon}'_{II\ (\text{plastic})}\phi}{f\ 2m\ \sigma_{yield}(1-\phi)}. \tag{17}$$

Upon simplification, where $2\dot{\varepsilon}_{II_{pl}}$ cancels out, we arrive at an analytical expression for the critical dilatancy:

$$D^{cr} = \frac{(1 - c/\sigma_{yield})\ (m+1)\phi}{f\ 2m\ (1-\phi)}. \tag{18}$$

Step 2: Numerical Validation of Analytical Solution. Next, we validate the analytical results through numerical simulations under the same simplifying assumptions. This step involves implementing a low permeability ($k_0 = 10^{-20}\ m^2$) and incompressibility with $\beta_s = \beta_f = 0$ and therefore $\alpha = B = 1$ (see details in Section 3.3.2).

Step 3: Effects of Pressure Diffusion with Dilatancy in the Incompressible Case. In the third step, we reintroduce the effects of pressure diffusion by increasing permeability to the magnitude of $k_0 = 10^{-17}\ m^2$. Similarly to the previous step, we assume unit Biot and Skempton coefficients ($\alpha = 1$, $B = 1$), which removes elastic storage due to solid and fluid compressibility, but does not eliminate pressure diffusion. This is because pressure diffusion in our model is governed by Darcy flow driven by pore-pressure gradients, and remains finite as long as permeability (k) and fluid viscosity (η_f) are finite. In this limit, the storage term becomes dominated by porosity changes associated with (de)compaction, rather than by elastic compressibility. This allows us to assess the influence of fluid flow on the interplay between dilatancy and compaction and to compare these results to the initial set of models with low permeability (Section 3.3.2) and the models without dilatancy (Section 3.2). The results of this set of experiments are detailed in Section 3.3.3.

Step 4: All Effects, Including Compressibility. Finally, we include all the physical terms, with the last step reintroducing compressibility effects. This setup incorporates the full range of processes affecting dilatancy and compaction interactions, allowing for a more realistic representation of the fault zone physics (see Section 3.3.4).

2.4 Model setup and boundary conditions

The 2D model setup is a simplified version of a natural strike-slip fault zone (Fig. 3a). The modeled fault width represents the numerically resolved shear zone in which deformation and slip localize. For computational reasons, this width is defined at the scale of a fault damage zone in nature ($250 - 500$ m). The fluid is allowed to flow both between inside and outside of this zone. The reference model (Fig. 3) consists of a dextral strike-slip fault (Fig. 3b), embedded in a poro-visco-elasto-plastic medium, and has a size of 120 km in the along strike direction and 30 km in the fault-normal direction, with an initial grid resolution of 500 m in both directions. The γ rate-strengthening exponent is defined to be high near the vertical boundaries of the model, and an order of magnitude lower in the middle of the fault (Fig. 3c). This rate-strengthening exponent affects the nucleation: the low γ ensures that the nucleation of the seismic events happens in the middle of the fault, where the stress is concentrated during the loading phase, while the higher γ near the boundaries guarantees that the rupture doesn't nucleate and propagate near the boundary.

For a coupled solid-fluid system, the pressure boundary conditions are defined for the difference between the total P^t and fluid P^f pressures. The initial condition for the fluid pressure is $P^f = P_{conf}$, where P_{conf} is the constant confining pressure, and we apply constant effective pressure (P_{eff}) at the boundaries:

$$P_{eff} = P^t - P^f. \tag{19}$$

The normal component of the solid velocity is assumed not to vary across the left and right model boundaries whereas the parallel velocity component is assumed to be zero, which allows natural conditions for strike-slip deformation on the fault. The model is loaded from the upper ($y = 0$) and lower ($y = L_y$) boundaries by applying a constant loading velocity (v_l). For the solid velocity, the horizontal component v_x^s equals to a constant loading velocity v_l = 3.15 cm yr^{-1}, and the vertical velocity v_y^s equals to zero. Fluid velocity boundary condition is impermeable on all boundaries.

This model setup allows earthquake cycle simulations in a relatively simple environment such that we can investigate the effects of different parameters on the evolution and slip behavior of the fault. Notably, the model formulation ensures that pore pressure never exceeds the total normal stress, such that the effective normal stress remains positive throughout the rupture evolution. Slip therefore proceeds in shear (mode II) along the fault plane. Table 1 shows the parameters for the reference model.

3 Results

We perform an extensive range of parameter tests to examine the effects on fault evolution and assess the numerical stability of the H-MEC code. Given the complexity of the governing equations, we apply simplifications to isolate the terms and investigate the impact of different parameters. First, we deactivate the dilation term to examine the general behavior of the model without dilation (Section 3.1). Secondly, we analyze the influence of fluid parameters (porosity and permeability) on the seismic slip mode in the absence of dilation (Section 3.2). Third, we explore the interplay between dilation and visco-plastic compaction using both the simplified approach derived in Section 2.3, and the full set of equations (Section 3.3).

3.1 General Model Behavior Without Dilatancy - Fluid-Driven Earthquake Cycles

For parameter choices that lead to instabilities, three distinct phases define the evolution of the fault in our models, also observed in Petrini et al. (2020) and Dal Zilio et al. (2022): (1) The pre-seismic loading phase, during which the fault is locked in the seismogenic zone while creeping occurs on the sides. During this stage, the visco-plastic compaction of fluid-filled porous media initiates pore fluid pressurization on the fault. The timescale for this phase ranges from years to hundreds/thousands of years, depending on model parameters. (2) The co-seismic phase, characterized by a developing shear instability and the propagation of seismic events as solitary fluid pressure waves on the timescale of milliseconds to seconds, while the slip rate on the fault accelerates from cm yr^{-1} to m s^{-1}. The term solitary wave here refers to nonlinear, self-reinforcing fluid pressure perturbations, that maintain their localized shape and amplitude as they propagate through the medium. Such behavior can arise when non-linear compaction-decompaction dynamics of the porous skeleton interact with dispersive effects associated with pore-fluid pressure diffusion and elastic coupling. The balance between these two processes prevents diffusive spreading and produces coherent traveling fluid pressure fronts, a mechanism also described in Dal Zilio et al. (2022). As these short timescales do not allow for any significant fluid pressure diffusion from the deforming fault zone, the visco-plastic compaction is compensated by the poro-elastic decompaction, resulting in increased pore-fluid pressure and reduced shear strength on the fault. This shear instability rapidly grows, leading to the propagation of a dynamic rupture manifesting as a fluid pressure wave. Seismic events nucleate in the middle of the fault due to the relatively large nucleation size affected by the rate-strengthening parameter (γ), while the fault keeps creeping outside the seismogenic zone. Simultaneously, the effective pressure ($P^t - P^f$) drops due to the poro-elastic response of the fault. (3) The post-seismic phase, when the increased fluid pressure is released over a post-seismic diffusion period, which gradually relaxes the co-seismic elastic decompaction. For simplicity, our models focus on stress and pressure evolution with time and neglect the related small porosity changes. The duration of the diffusion period depends on the permeability, and can span years or longer. Once fluid pressure is released, the self-pressurization on the deforming fault may resume, initiating new seismic cycles.

Our adaptive time-stepping algorithm enables the code to use time steps in the order of years between

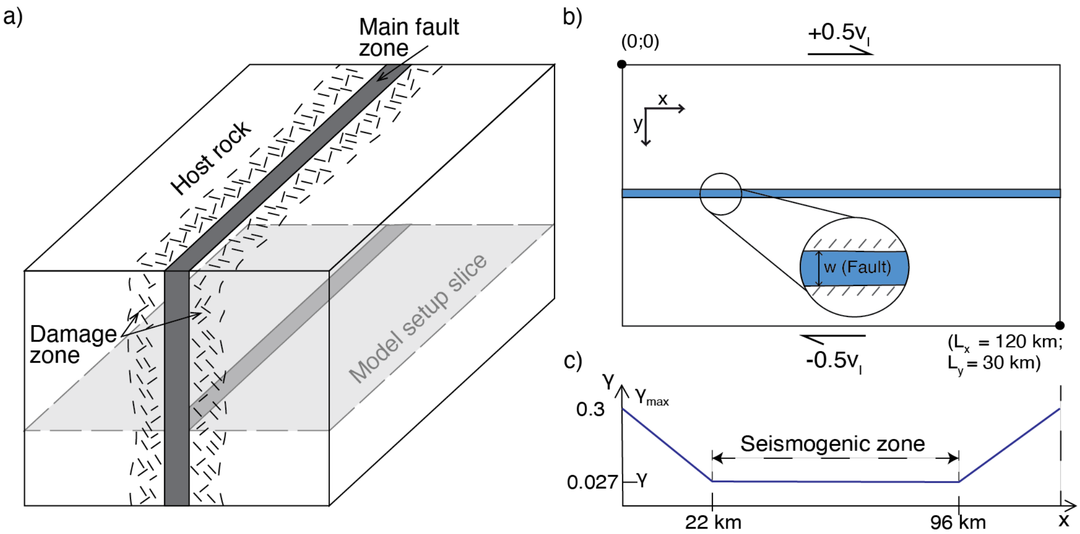

Figure 3 Layout of model setup. a) Schematic sketch of a strike slip fault zone. b) In plane fault embedded in a homogeneous poro-visco-elasto-plastic media. The domain is loaded from the top and bottom boundaries. c) Setup of γ rate-strengthening parameter.

Parameter	Symbol	Value
Domain size (x)	L_x	120 km
Domain size (y)	L_y	30 km
Grid resolution	dy, dx	500 m × 500 m
Fault width	w	dy or dy/2
Reference porosity	ϕ_0	1%
Cohesion	c	3 MPa
Reference friction	f	0.3
Shear modulus	G	30 GPa
Fluid compressibility	β_f	$4 \times 10^{-10}\,\mathrm{Pa}^{-1}$
Solid compressibility	β_s	$2.5 \times 10^{-11}\,\mathrm{Pa}^{-1}$
Confining pressure	P_{conf}	10 MPa
Effective pressure	P_{eff}	60 MPa
Minimum rate strengthening exponent	γ	0.027
Maximum rate strengthening exponent	$\gamma_{\max}$	0.3
Fluid density	ρ_f	$1000\,\mathrm{kg/m^3}$
Solid density	ρ_s	$3000\,\mathrm{kg/m^3}$
Fluid viscosity	η_f	$10^{-3}\,\mathrm{Pa \cdot s}$
Solid viscosity	η_s	$10^{23}\,\mathrm{Pa \cdot s}$
Characteristic velocity	V_{ch}	$0.5 \times 10^{-9}\ \mathrm{m/s}$
Reference strain rate	ε_0	$V_{\mathrm{ch}}/(2 \cdot dy)$

Table 1 Reference parameters. All parameters are applied to both fault zone and surrounding materials, unless otherwise noted.

seismic events during the interseismic period, and accurately resolve dynamic rupture propagation with time steps on the order of milliseconds. The average recurrence interval of seismic events varies between 50 to 500 years depending on the model parameters, and the slip rate of regular earthquake events ranges between $0.3 - 3\,\mathrm{m\,s^{-1}}$. The recurrence time of seismic events is affected by both physical and numerical parameters, including permeability, porosity, fault width and grid step size (Sections A and 3.2).

This method effectively reproduces the entire slip spectrum (Fig. 4). By systematically testing physical parameters, regular earthquake cycles can be modeled with relatively constant recurrence times and realistic slip rates (Fig. 4a). The models also reproduce slow slip phenomena (Fig. 4b): slow slip events last from hours to days, with maximum slip rates of 10^{-6} to $10^{-4}\,\mathrm{m\,s^{-1}}$, as well as aseismic creep (Fig. 4d), representing transient deformation along the fault with no associated seismic activity. Some models exhibit a temporal shift in slip mode (Fig. 4c): initially, regular earthquakes are observable in the early stages of model evolution. However, the fluid pressure always increases due to the chosen low permeability, which in turn results in the decrease of the effective pressure along the fault. This means that the fluids in the fault cannot depressurize efficiently, which causes a transition from regular earthquakes to slow slip events, and ultimately, to aseismic creep in the later stages of the model run. The slip behavior of the models highly depends on fluid parameters (permeability, porosity, fluid compressibility (Dal Zilio et al., 2022). The effects of fluid parameters, porosity, and permeability on the seismic cycles are described in Section 3.2, focusing on separating the poro-elastic response of the fault from visco-plastic compaction. The dilational effects in response to compaction and fluid pressurization are described in Section 3.3.

3.2 Influence of permeability, porosity, and fault width on seismic slip behavior without dilatancy

To evaluate the conditions under which different fault slip modes occur, we completed a systematic parameter test of permeability (k) and porosity (ϕ_0) (Fig. 5) for two different fault widths ($w = dy$ and $w = dy/2$). A range of permeability values were used (~ 4 orders of magnitude, between 10^{-19} and 10^{-15} m^2) at two end-member porosities (1% and 5%) (Peacock et al., 2011; Tewksbury-Christle and Behr, 2021). The different colors in Fig. 5 indicate the observed slip mode throughout at least five regular earthquake cycles (for fast slip).

The numerical experiments presented in Fig. 5 illustrate that changing fluid parameters results in different types of slip behaviors. With the fault thickness set to $w = dy$ (Fig. 5a), persistent fast events do not occur over the permeability-porosity space implemented. For the permeability values of $k < 10^{-17}$ m^2 and 1 % porosity, all models eventually transition to aseismic creep, starting with either fast or slow events (Fig. 5c). At higher permeabilities, aseismic creep is observed without transient activity (Fig. 5f). The transition from the transient slip regime to the aseismic creep regime at higher porosity ($\phi = 5\%$) requires around an order of magnitude higher ($k = 10^{-16}$ m^2) permeability (Fig. 5d).

Fig. 5b presents the results of numerical experiments with the narrower fault width ($w = dy/2$). For permeabilities below approximately $k \approx 5 \times 10^{-18}$ m^2, the models show the same transient behavior from regular earthquakes to aseismic creep, with model evolutions similar as illustrated in Figs. 5c, d. In these models, lower permeabilities allow fluids to pressurize easily initially, triggering the first event. However, after the first event, the low permeability hinders pore pressure diffusion during the interseismic period. In such cases, the effective pressure fails to recover past a few minor transient events, prompting the fault to transition into aseismic creep behavior. Conversely, at the highest implemented permeabilities ($k > 10^{-16}$ m^2), similarly to the previous case (Fig. 5a) aseismic creep becomes the dominant slip mode (Fig. 5f), or transient behavior (in case of $\phi_0 = 5\%$). This is because the high permeability prevents the pore fluid from pressurizing in the first place due to fast pressure diffusion. Between these two permeability values (10^{-18} m$^2 < k < 10^{-17}$ m^2 with $\phi = 1\%$ and 10^{-17} m$^2 < k < 10^{-16}$ m^2 with $\phi = 5\%$), a 'sweet spot' occurs in which regular, persistent, earthquake cycles are generated, with relatively constant recurrence intervals within each model run (Fig. 5e). These seismic events follow the behavior described in Section 3.1.

The two slip regime diagrams in Fig. 5a, b, highlight the influence of fault zone thickness. With the wider fault ($w = dy$), the peak slip rates are lower compared to the thinner fault ($w = dy/2$). This is partly because the fluid pressure diffusion is slower across a wider fault, as the pressure perturbation takes a longer time to spread across the larger fault area. Additionally, since the shear modulus was not changed with fault width change, the total slip per unit area is smaller in case of a wider fault, and the strain is distributed over a larger area, as the increase in the fault width means an increase in the area over which strain is distributed. These factors result in overall slower slip events, lower peak slip rates, and a tendency toward transient behavior or aseismic creep, with the absence of recurring fast or slow events.

3.3 Effects of Dilation

3.3.1 Step 1: Analytical Solution for Critical Dilatancy

Using reference parameters in Equation 18, $c = 3.3 \times 10^6$ Pa, $\sigma_{yield} = 6.6 \times 10^6$ Pa, $m = 2$, and $f = 0.3$, $\phi = 1\%$, the critical dilatancy coefficient was calculated as $D^{cr} = 0.012$. As shown in Figure 6a, the analytical solution predicts that D^{cr} highly depends on porosity.

3.3.2 Step 2: Numerical Validation of Analytical Solution

The results of a set of numerical experiments under the same simplifying assumptions as the analytical model are also plotted in Figure 6a. These experiments tested different dilatancy coefficients at four different porosity values (1%, 3%, 5%, 7%). The numerical model predicts the same critical dilatancy needed to produce fast slip as the analytical solution, with transitions between slip modes occurring at similar D^{cr} values for each porosity (Fig. 6a). Interestingly, slow slip events appear at dilatancies close to the analytical solution ($D^{cr} - D < 0.01$), while the fast slip regime is observed at dilatancies $D^{cr} - D \approx 0.01$, and an aseismic creep regime is detected at dilatancies $D > D^{cr}$. With higher porosities, the transition between slow and fast slip events is shifted to higher dilatancies (Fig. 6a), consistent with the analytical prediction of the dependency of D^{cr} on porosity.

The general fault evolution in these models follows the same three phases described in Section 3.1: (1) During the pre-seismic phase, fluid pressurization due to the visco-plastic compaction dominates as the fault is loaded. (2) In the co-seismic phase, shear instability grows into a seismic event , due to increased fluid pressure in cases where the dilatancy cannot counteract the effect of the visco-plastic compaction, and the seismic event can develop as described in Section 3.1. (3) During the post-seismic phase, fluid pressure dissipates slowly

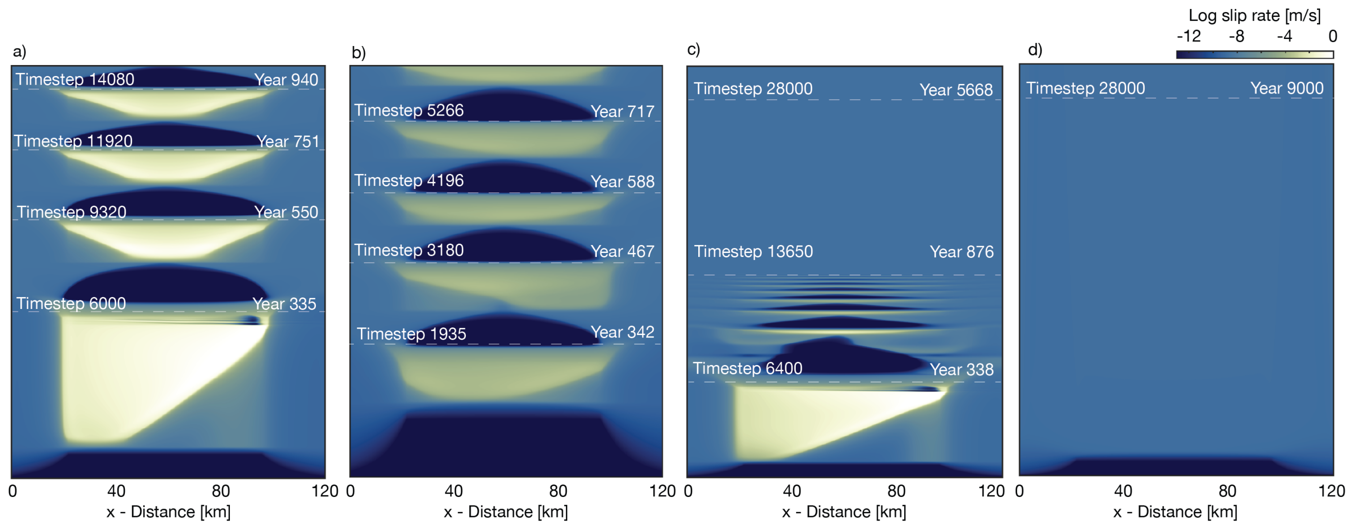

Figure 4 Example models showing the slip rate evolution of the fault for four different types of slip modes. X axis shows distance along the fault, y axis shows time step (with variable size as a result of the adaptive time stepping algorithm. The color bar shows the logarithm of the slip rate. a) Regular earthquake cycles. b) Slow slip events. c) Temporal shift of slip mode from regular earthquakes to slow slip events to aseismic creep. d) Aseismic creep without associated seismic activity.

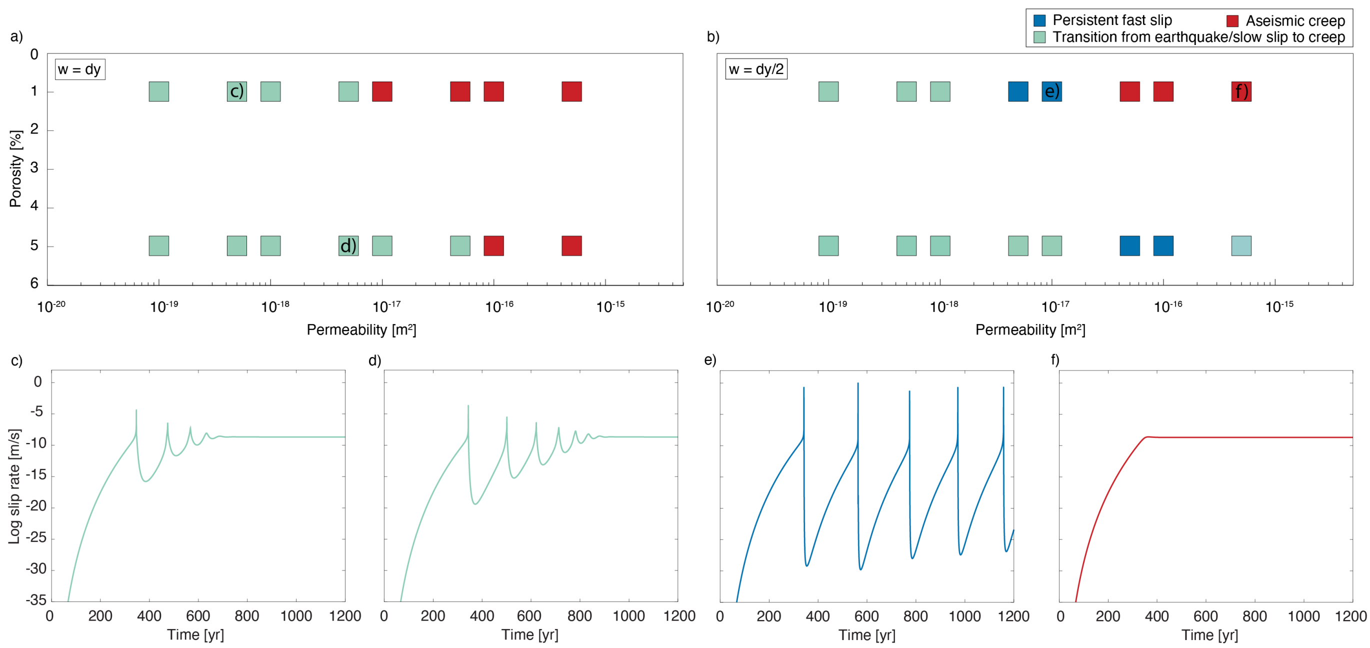

Figure 5 Effects of permeability (k) on log scale and porosity (ϕ) on the slip mode. a)-b) Comparison of porosity and permeability at two different fault widths. Colors indicate the slip mode of the fault, blue symbolises fast slip, red symbolises aseismic creep, green symbolises a transient behaviour from fast to slow slip to stable creep. c)-f) Examples of temporal evolution of maximum slip velocity during different slip responses. c), d) show transient behaviour, e) shows fast slip, f) shows stable creep.

over hundreds of years, stabilizing the fault and transitioning it to aseismic creep. Due to the intensionally prescribed low permeability, only one seismic event can occur (Fig. 7, blue line). The inclusion of dilatancy thus does not alter the general fault evolution but does influence slip behavior, particularly near the critical dilatancy.

The slow slip events in this set of numerical experiments occur when D is close to D^{cr}. These events exhibit slip rates of 10^{-6} to 10^{-4} m s^{-1}, reflecting an intermediate state where dilatancy partially offsets compaction but does not fully stabilize the fault. At the end of these slow slip events the fault transitions to aseismic creep (Fig. 7, orange line). In contrast, when $D > D^{cr}$, dilatancy fully counteracts compaction, preventing fluid pressure from reaching levels sufficient to trigger shear instability, thus resulting in aseismic creep throughout the fault's evolution (Fig. 7, red line).

These results confirm that the numerical model, under the same assumptions, reproduces the critical dilatancy threshold and slip mode transitions predicted by the analytical solution. Additionally, the numerical model captures slow slip behavior near D^{cr}, which highlights the ability of the model to represent

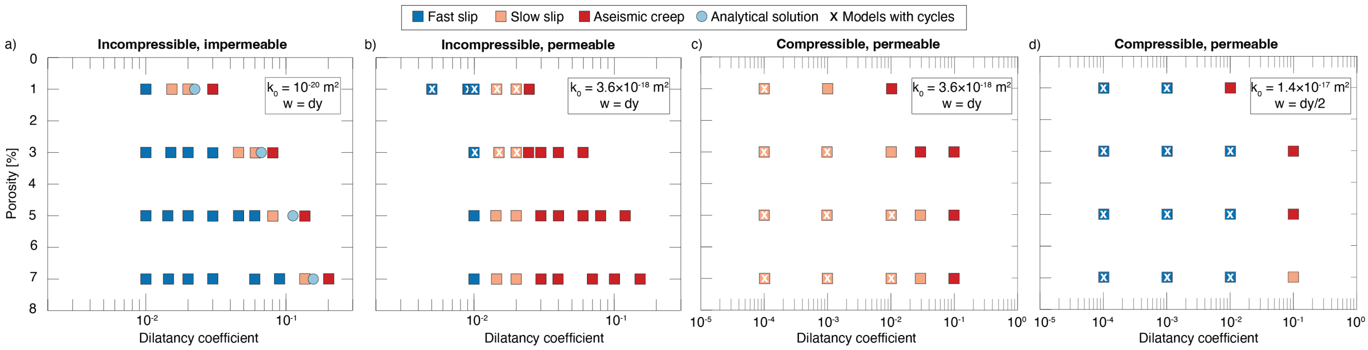

Figure 6 Effects of porosity (ϕ) and dilatancy coefficient (on log scale) on the slip response of the fault - subplots a and b with incompressibility assumption, subplots c and d are fully compressible (with different fault widths). Marker colors show different initial slip responses: blue: fast slip, red: aseismic creep, orange: slow slip, light blue: analytical solution calculated from Eq. 18. a) Relationship between porosity and dilatancy coefficient at low permeability with incompressibility assumption. b) Relationship between porosity and dilatancy coefficient at high permeability with incompressibility assumption. X indicate models with fast or slow slip cycles. Section 3.3.3 details the description of this subset of models. c) Relationship between porosity and dilatancy coefficient in the fully compressible case with $w = dy$. d) Relationship between porosity and dilatancy coefficient in the fully compressible case $w = dy/2$. Section 3.3.4 details the description of the two compressible, impermeable subsets of models.

a broader spectrum of fault slip behaviors compared to the analytical solution.

3.3.3 Step 3: Relationship between (de)compaction and dilatancy in an incompressible, permeable fault

Building on the results from Step 2, we conducted a second suite of numerical experiments to evaluate the role of dilatancy in the presence of fluid pressure *and* diffusion. Compared to Step 2, permeability was increased by two orders of magnitude ($k = 7.2 \times 10^{-18}$ m^2), allowing the divergence of the Darcy velocity (left side of Eq. 4) to become significant. The models retained the assumption of incompressibility ($\beta_s = \beta_f = 0$). The analytical solution for critical dilatancy (D^{cr}) provided a baseline for comparison, as in Step 2.

Figure 6b shows that under these more realistic conditions, the critical dilatancy coefficient required to permit fast events shifts to much lower values compared to Step 2. Specifically, faults with dilatancy coefficients $D > 10^{-2}$ no longer exhibit fast slip behavior, even at low porosities. This leftward shift reflects the role of fluid diffusion in mitigating pore fluid pressure buildup caused by compaction (similar to effects described in Section 3.2). At higher permeability, fluid pressurization is more difficult, reducing its destabilizing effects and therefore requiring much lower dilatancy to stabilize the fault. In contrast, low permeability in Step 2 restricted fluid diffusion, amplifying compaction effects and requiring higher dilatancy coefficients for fault stabilization.

Similar to the models in Step 2, this suite again shows variations in slip behaviors near the transition to fast slip, and these variations depend on porosity. At low porosities (1% and 3%), the fault exhibits fast slip cycles for $D \leq 0.01$, with fault evolution following the three-phase sequence described in Section 3.1. At near-critical dilatancies ($0.016 \leq D \leq 0.018$) and 1% porosity, the fault transitions to slow slip events, with slip rates of 10^{-6} to 10^{-4} m s^{-1}, reflecting partial stabilization by dilatancy. For 3% porosity, slow slip events give way to aseismic creep after 1-5 slow slip events. At 5% and 7% porosities, fault behavior remains consistent with Step 2: after one fast or slow slip event, dilatancy fully stabilizes the fault, resulting in aseismic creep.

These results demonstrate that permeability modifies the balance between dilatancy and compaction, shifting the slip mode transitions to lower dilatancy coefficients. While porosity plays a weaker role in setting the boundary between transient and seismic creep, it does influence the number and type of slip events prior to stabilization in the boundary region.

3.3.4 Step 4: Relationship between (de)compaction and dilatancy in a fully compressible and permeable fault

Building on the results from Steps 2 and 3, we now incorporate all physical terms into the model, including compressibility effects for both the solid and fluid phases (β_f and β_s values listed in Table 1). Fig. 6c, d summarize the slip response across the tested range of dilatancy coefficients and porosities for a constant permeability of $k = 3.6 \times 10^{-18}$ m^2 in case of $w = dy$, and $k = 1.4 \times 10^{-17}$ m^2 in case of $w = dy/2$.

For the case of a wider fault ($w = dy$), only slow transient slip or aseismic creep is observed (Fig. 6c), consistent with the results shown in Fig. 5a (without dilatancy) in which compressibility effects suppress fast fault slip due to significant fluid volume reduction during pressurization. For most dilatancy values, initial transient slow slip events still occur in these models, as expected for these permeability-porosity choices based on Fig. 5a. However, dilatancy coefficients greater than 10^{-2} (at low porosity) and 10^{-1} at high porosity led to suppression of any transient fault slip. Thus, including high dilatancy coefficients leads to a leftward shift in the boundary between transient slow slip and aseismic slip in Fig. 5a, with the magnitude of this shift weakly de-

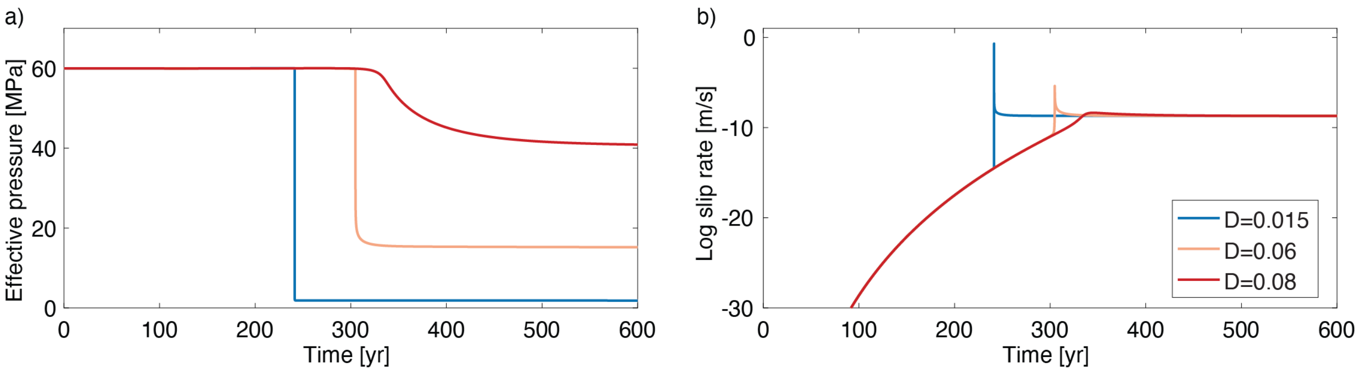

Figure 7 Examples of the different slip modes in case of incompressible and impermeable fault: fast slip (blue line), slow slip (orange line) and aseismic creep (red line). a) and b) present the effective pressure evolution, and the slip rate evolution through time, respectively.

pendent on porosity.

Using the narrower fault width ($w = dy/2$), the fast slip regime appears again at dilatancy of $D = 10^{-3}$ for 1% porosity, and at $D = 10^{-2}$ for porosities of 3%, 5% and 7% (Fig. 6d). Similarly to Section 3.2, the narrower fault enables faster slip events and higher slip rates for the permeability value chosen here. In comparison to Fig. 5b, we see that the fast slip that is predicted at 1% porosity for our selected permeability is suppressed to aseismic creep at dilatancy coefficients above 10^{-2}. This again suggests that a weakly porosity-dependent, leftward shift in the boundary between fault slip modes should occur at relatively high dilatancy coefficients.

The evolution of effective pressure for both fault widths at 1% porosity with four different dilatancy coefficients is shown on Fig. 8a-b. In both cases, at $D = 10^{-2}$ the fault remains in aseismic creep throughout its evolution because dilatancy has suppressed transient events. For the wider fault ($w = dy$, Fig. 8a), lower dilatancy coefficients ($D = 10^{-3}$) result in slow slip events before transitioning to aseismic creep behavior. For $D = 10^{-4}$ and $D = 0$, the fault hosts multiple slow slip events, with decreasing effective pressure during slip episodes and gradual stabilization. The difference in the model evolutions is small, with the timing of the first two events only differing by 7-10 days. In contrast, the use of the narrow fault width ($w = dy/2$) results in fast events. The models show recurring fast events, and identical behavior at $D = 10^{-4}$, $D = 10^{-3}$, and $D = 0$. The similarity between models without dilatancy and models with relatively low dilatancy indicates the lesser role of dilation compared to compressibility and compaction in both cases.

4 Discussion

4.1 Effects of fluid properties on fault slip without dilatancy

In Section 3.2 we examined the effects of compaction/decompaction and fluid flow on fault slip behavior in the absence of dilatancy, examining how permeability, fault zone width, and porosity govern the development of fluid overpressure and control transitions between seismic and aseismic slip. Our parameter study demonstrated that for a porosity range of 1-5%, fast slip events (slip velocities up to the magnitude of 10^0 m s^{-1}) are only observed over a narrow permeability window, $k \approx 10^{-17}$ to 10^{-16} m^2, and exclusively for the narrower fault width. In these models, increasing permeability above 10^{-16} m^2 enhances Darcy velocity (following Equations 3 and 4), reducing fluid pressurization and thus favoring aseismic slip. Conversely, at permeabilities below 10^{-17} m^2, fluid becomes over-pressurized due to limited diffusion, reducing effective stress and suppressing dynamic rupture due to permanent fluid-pressure-induced weakening. When using the wider fault, at both 1% and 5% porosities, the boundary between transient and aseismic behavior slightly shifts to higher permeabilities by about half an order of magnitude. Fault zone width influences the storage capacity of the system and controls the magnitude of pore pressure changes during deformation (Faulkner et al., 2010; Cappa, 2011). Here the storage capacity β^* is defined as:

$$\beta^* = \phi\left(\beta_f - \beta_s\right) + \left(\beta_d - \beta_s\right). \qquad (20)$$

Thus, an increase in porosity implies an increase in local storage capacity. Additionally, porosity also influences permeability (Eq. 11), and therefore the effective pressure distribution within the fault zone. Although β^* is a material property independent of fault width, a wider fault implies that the pore pressure changes generated by compaction are distributed over a larger volume. In addition, wider faults have a larger total pore volume and enhance permeability pathways, promoting more efficient pressure diffusion. These effects together lead to the absence of recurring fast events in all wide fault models.

In addition to permeability and fault width, porosity further modulates slip behavior by influencing compaction and decompaction efficiency. Higher porosity reduces compaction and enhances fluid accommodation, thereby modifying the pore pressure evolution during slip. For instance, achieving recurring seismic events at 5% porosity with the narrow fault required higher permeability compared to the 1% porosity case (Fig. 5b). This reflects the dual role of porosity in both controlling compaction rates and modulating the

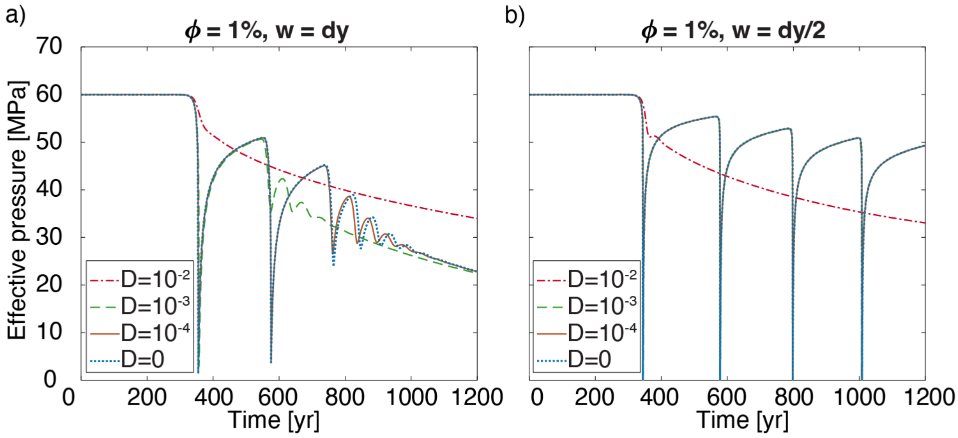

Figure 8 Effective pressure evolution in time on the fault, in a fully compressible medium in case of ϕ = 1%. a) With the use of $w = dy$. b) With the use of $w = dy/2$. Line colors indicate different dilatancy coefficients.

Skempton's coefficient, B, which governs the magnitude of fluid pressure response. In our models, the Skempton's coefficient is $B = 0.226$ for 1% porosity, and $B = 0.233$ for 5% porosity. Since Equation 4 includes the reciprocate of B, a higher B implies a smaller effective pressure drop during an event, favoring slower slip or aseismic deformation. Additional factors, such as fluid and solid compressibility, and dilatancy (see Section 4.2) can also modify slip mode by modifying the Skempton's coefficient, as discussed in Dal Zilio et al. (2022). In that study, slow slip events were observed at higher fluid compressibility than our reference value (β_f, Table 1), and at a higher porosity of 10%.

The relatively narrow parameter range producing recurring fast slip events in the narrow fault width case reflects the simplifications in our model formulation, in which material properties (e.g. porosity and permeability) are held constant in space and time. However, variations in these parameters as well as in fluid compressibility can broaden the instability regime (Dal Zilio et al., 2022), suggesting that fluid-driven instabilities may dominate over a wider range of natural conditions than captured by the models in this study. Taken together, these results show that even in the absence of dilatancy, fault slip behavior is highly sensitive to fluid-related properties and fault geometry. Compaction-driven pore pressure increases can promote dynamic slip under specific permeability and porosity conditions, while enhanced pressure diffusion or fluid storage capacity tends to stabilize slip.

4.2 Role of Dilation

Shear-induced volumetric expansion (dilatancy) has long been recognized as a potentially stabilizing mechanism in laboratory-scale, fluid-bearing faults and natural fault systems (Nur, 1972; Rudnicki and Chen, 1988; Segall and Rice, 1995; Samuelson et al., 2009; Segall et al., 2010). Dilatancy coefficients measured in the lab on granular fault gouges are typically in the range of $D \sim 10^{-3}$ to 10^{-5} (Segall and Rice, 1995; Samuelson et al., 2009; Beeler et al., 2018; Brantut, 2020). Several studies have suggested that dilatancy coefficients in this range can influence fault slip behavior by reducing pore fluid pressure during shear and inducing dilatant hardening (Segall and Rice, 1995; Rudnicki and Chen, 1988; Proctor et al., 2020; Aben and Brantut, 2021). Although the dilatancy parameter in our model differs in formulation from the rate-and-state dilatancy parameter of Segall and Rice (1995), the comparison is still applicable here as an order-of-magnitude reference. In our formulation, dilatancy is a constant coefficient linking plastic shear strain rate to volumetric expansion, whereas Segall and Rice (1995) describes dilatancy as a dynamically evolving process within a rate-and-state dependent framework. Both approaches nevertheless represent the same physical mechanism of shear-induced pore-space creation and associated pore-pressure reduction. Recent work further suggests that porosity and compaction state may directly influence fault strength, providing an additional way by which dilatancy and compaction can stabilize or weaken slip (Sarma et al., 2025).

The analytical solution derived for the critical dilatancy coefficient D^{cr} discussed in Section 3.3.1 provided a framework to predict the transitions in fault slip mode under incompressible conditions with negligible fluid pressure diffusion. This predicted that dilation can suppress fast slip, but only at relatively high dilatancy coefficients ($D > 10^{-2}$) that exceed values typically observed in laboratory experiments. Our numerical models using the same assumptions, with a wide fault width, confirmed this prediction, but also showed additional complexity near D^{cr}, including slow slip events that reflect slight stabilization by dilatancy at the transition from fast to aseismic slip. Introducing fluid pressure diffusion at the same fault width broadened the range of fault behaviors and shifted D^{cr} to slightly lower values by reducing compaction-driven pore pressure buildup, although dilatancy coefficient values needed to suppress transient slip ($D > 10^{-2}$) still remained higher than typical laboratory estimates. In models incorporating solid and fluid compressibility, dilatancy coefficients less than $D = 10^{-2}$ had no significant effect on the model behavior compared to the compressible cases with no dilatancy. At $D > 10^{-2}$, the boundary between transient and aseismic creep shifts to slightly lower permeability values in both wide and narrow fault configurations. This shift reflects the larger pore volume reservoir introduced by dilation, which delays fluid pressurization and thus requires slower pressure diffusion (i.e. lower permeability) for dynamic rupture to initiate.

Collectively, these results imply that dilatant hardening is unlikely to modulate fault slip in compressible, permeable fault systems unless the dilatancy coefficient exceeds $D \sim 10^{-2}$. Below this threshold, fault slip mode is more strongly governed by pressure diffusion (controlled by permeability and fault width) and pore compressibility.

4.3 Comparison to Rate and State Friction Models

Experimental studies over the past several decades have demonstrated that frictional resistance evolves with both the rate of deformation and the sliding history of the fault surface (Ruina, 1983; Scholz, 1998; Rice, 2006; Niemeijer and Spiers, 2007). This behavior is captured by the rate- and state-dependent friction (RSF) formulation (Dieterich, 1978; Ruina, 1983; Marone, 1998; Scholz, 1998), which has become the standard framework for modeling fault shear resistance at slip rates ranging from tectonic plate rates of 10^{-9} m s^{-1} to about 10^{-3} m s^{-1}. In this formulation, the parameter $a - b$ governs whether a fault exhibits velocity-strengthening ($a - b > 0$) or velocity-weakening ($a - b < 0$) behavior, which in turn controls fault stability. However, while RSF is effective for modeling fault slip, it does not inherently account for the physical mechanisms of dynamic weakening and evolution of the state variable. Physical mechanisms proposed in the past include contact aging and asperity interactions (Dieterich, 1978; Ruina, 1983), thermal pressurization (Rice, 2006; Viesca and Garagash, 2015), flash heating (Tsutsumi and Shimamoto, 1997; Goldsby and Tullis, 2011), shear-induced dilation or compaction (Segall and Rice, 1995; Marone, 1998), and microphysical processes such as pressure solution and granular flow (Niemeijer and Spiers, 2007; van den Ende et al., 2018). In addition, alternative constitutive laws from microphysical models have been proposed to model instability (Shimamoto and Noda, 2014; Chen and Niemeijer, 2017).

Classical RSF models predict seismic instability at rate- or slip-weakening regimes, whereas velocity-strengthening faults are expected to exhibit stable slip under constant effective stress (Rudnicki and Chen, 1988; Segall and Rice, 1995). Reduced effective normal stress due to elevated pore pressure is commonly associated with aseismic behavior in these models. Consistent with these results, our simulations exhibit creep behavior under high pore pressure conditions (e.g. Fig. 5). However, a key distinction in our framework is that effective stress is not prescribed, but evolves dynamically throughout the model run, due to hydro-mechanical coupling. Consequently, pore fluid pressure increases weaken the fault, enabling dynamic slip even for intrinsically rate-strengthening rheologies.

Our study builds on this body of work, and on recent fully coupled fault models (e.g. Ciardo and Lecampion, 2019; Parez et al., 2023) by introducing a novel formulation that explicitly links the evolution of frictional strength to fluid pressurization and local porosity changes, governed by shear-induced dilation and compaction. In our model, the rate-strengthening parameter γ serves as an analog to the direct effect parameter a in RSF formulations, capturing the dependence of friction on instantaneous changes in slip velocity. However, unlike RSF, the weakening behavior in our model is not governed by phenomenological state variables but emerges from the coupled evolution of fluid pressure, effective stress, and local dilatancy. By incorporating these interactions into a coupled hydro-mechanical continuum framework, our model provides a physical mechanism for the dynamic weakening observed in fluid-bearing fault systems. This approach not only reproduces the same slip modes predicted by RSF, but also captures additional phenomena, such as the transition from velocity-strengthening to velocity-weakening behavior due to fluid pressurization. Moreover, it aligns with experimental observations and prior models that emphasize the critical role of fluid dynamics in controlling fault slip behavior (e.g. Sibson, 1992a; Segall and Rice, 1995; Beeler et al., 2018; Proctor et al., 2020; Farge et al., 2021; Yang and Dunham, 2021; Dal Zilio et al., 2022).

4.4 Implications for natural fault zones

Our findings have important implications for understanding slip behavior in natural fault systems where compaction, permeability, and compressibility interact to control effective stress. The dynamics discussed above may help explain spatial and temporal variability in natural seismicity, including slow slip events, migrating seismic tremor or earthquake swarms, and episodic fault activity associated with natural or anthropogenic fluid injection (e.g. Ide, 2010; Shelly and Hill, 2011; Ellsworth, 2013; Stanton-Yonge et al., 2025). Observations from exhumed faults commonly show evidence for heterogeneous permeability, fluid-pressure compartmentalization, and transient fluid migration, supporting the idea that such fluid-mechanical feedbacks are widespread (e.g. Sibson, 2017; Muñoz-Montecinos and Behr, 2023; Fagereng et al., 2017; Cox, 2005). In this context, the deformation regime in our models differs from the shallow, well-drained fault behavior commonly inferred from laboratory experiments, but is more comparable to experiments conducted under undrained or poorly drained conditions. The simulations here show a compaction dominated, fluid-rich regime in which pressure-driven deformation can promote transient pore-pressure build-up and reduced effective stress at slip initiation. These conditions may be relevant at low-permeability conditions, for example at clay-rich faults, where fluid diffusion is limited and fluid pressurization is expected. Several authors advocated shear-induced compaction on the bases of experimental (e.g. Proctor et al., 2020; Aretusini et al., 2021) and theoretical studies (e.g. Iverson, 2005; Goren et al., 2010).

Shear-induced dilatancy adds another layer of complexity. Although our results suggest that dilatant strengthening significantly affects slip behavior only when the dilatancy coefficient exceeds values typically estimated in laboratory settings, natural faults may locally or transiently exhibit higher effective dilatancy. Zones of distributed micro-cracking or shear banding, rupture-front dilational damage, or brecciation due to hydrofracture can accommodate large volumetric strain during shear (e.g. Sibson, 1986; Brantut, 2021; Woodcock et al., 2007; Muñoz-Montecinos et al., 2021; Sibson, 1990). High interface roughness or mismatched asperities may further enhance dilation as slip locally opens the fault surface (Caniven et al., 2021; Sibson, 1985). Thus, even if the average dilatancy coefficient of a mature fault core remains low, spatially localized or temporally transient episodes of high dilatancy could still meaningfully influence rupture dynamics through their effect on fluid pressure. Ultimately, our findings reinforce the view that fluid-mechanical coupling—not just frictional properties—plays a central role in governing the spectrum of fault slip behaviors observed in many active fault systems.

4.5 Model limitations and future work

While our models capture a broad spectrum of fault slip behaviors and provide valuable insights into the interplay between compaction-driven fluid pressure, dilatancy, and compressibility, they have several limitations. First, permeability and porosity are held constant throughout the simulations, whereas in natural fault zones, these properties evolve during deformation due to fracturing, healing and sealing, and/or diagenetic or metamorphic reactions (Rutqvist, 2012; Audet and Bürgmann, 2014). Second, the dilatancy coefficient is modeled here as a constant, and dilatancy rate only depends on the plastic strain rate, whereas in reality, dilatancy evolves with strain and confining pressure (Segall and Rice, 1995; Brantut et al., 2018). Third, our models do not account for variations in confining pressure with depth, which would be particularly important for dipping faults in layered or anisotropic lithologies. Depth-dependent pressure gradients influence fluid migration, permeability, and the magnitude of effective stress, potentially altering the stability regime of faults (Zhu et al., 2020). Fourth, the models assume simplified boundary conditions and spatial homogeneity, whereas natural faults often exhibit complex stress distributions, lithological heterogeneities, and irregular geometries. Fifth, our analysis assumes fluid-saturated conditions. We note that in the absence of fluids, or under dry fault conditions, the poro-mechanical feedbacks explored here would be largely absent. Although truly dry conditions are likely rare in the upper crust, especially at seismogenic depths, addressing this contrast highlights the central role of fluids in modulating fault slip behavior. Finally, our simulations are two-dimensional, inherently limiting their ability to replicate the three-dimensional nature of stress interactions and fluid flow in natural fault systems (Jiang et al., 2022). Incorporating dynamic evolution of dilatancy, permeability and porosity, as well as accounting for depth-dependent confining pressure and expanding to three-dimensional models, would enhance the applicability of these findings to natural fault systems.

5 Conclusions

We used the Hydro-Mechanical Earthquake Cycles (H-MEC) code to model earthquake cycles on a strike-slip fault. A novel plasticity model was introduced, to link the evolution of frictional strength to fluid pressurization. Our models capture a broad range of fault slip behavior from seismic to aseismic slip, including slow slip events and stable creep. We described the evolution of fluid-driven seismic events, and investigated the influence of fluid parameters, such as porosity and permeability, as well as fault width, on the seismic slip mode in the absence of dilatancy. Then, we analyzed the role of dilatancy compared to the visco-plastic compaction, poro-elastic (de)compaction, and fluid-pressurization in a step-wise manner, incrementally introducing complexity into the models. Our findings show that porosity and fluid pressurization highly impact the seismic and aseismic slip modes in the presence of dilatancy. In a compressible, dilatant, and permeable fault, the models are unable to capture the fast slip with the use a wide fault. However, fast slip events are observed along the narrow fault, highlighting the importance of compressibility and poro-elastic storage. Building on previous studies, our work demonstrates how seismic ruptures initiate due to pore pressure variations driven by compaction processes. By incorporating all these effects in a coupled hydro-mechanical visco-elasto-plastic continuum framework, the models presented here reproduce the slip modes predicted by rate and state friction laws, and highlight the observation from previous studies that suggested a significant role of fluid dynamics in fault slip behavior.

A Scaling physical parameters with grid step size (without dilatancy)

Understanding how the scaling of specific parameters affects the results is crucial for evaluating the Hydro-Mechanical Earthquake Cycle (H-MEC) code. This includes examining the convergence of multiple parameters such as resolution, slip rate, yield stress, effective pressure, total pressure, fluid pressure, and the timing of the first seismic event. In finite difference methods, the resolution affects the accuracy, stability, and convergence of the numerical solution by impacting the approximation of derivatives; therefore, the grid step size must be sufficiently small to resolve the cohesive zone length during rupture simulation (Day et al., 2005). In nature, physical parameters also depend on the length scale, including permeability. In order to introduce scaling relationships we took into account that the width of the highly localized pressurized slip zone during the co-seismic phase always comprises 1-2 vertical grid step sizes, which makes both the timescale of pressure diffusion and the compaction viscosity depending on grid resolution. In order to compensate these two effects, we implemented the following scal-

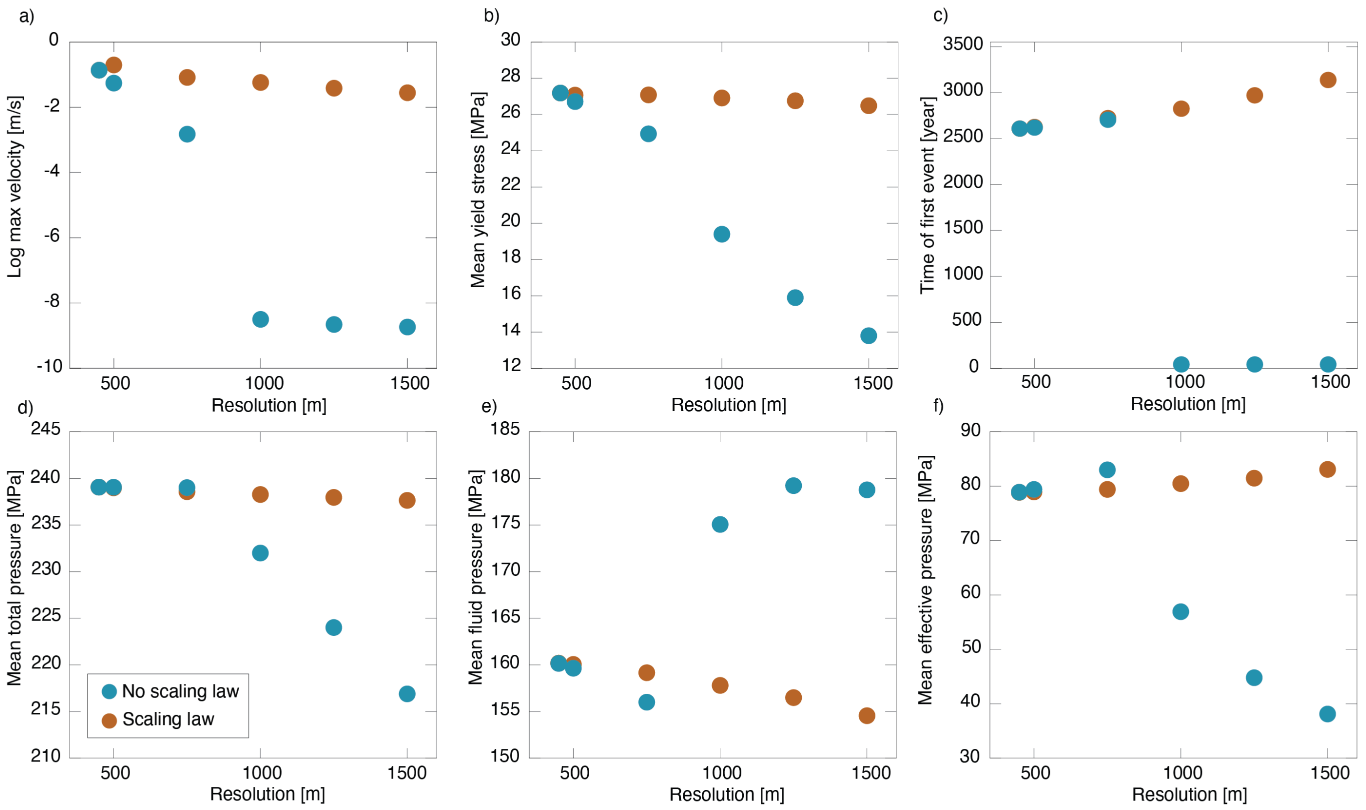

Figure 9 Results of the resolution tests. The blue dots show model results without the implemented scaling law, the brown dots show model results with the use of the scaling laws (Eqs. 21, 22). X axis always shows the used resolution, y axis shows a)-f) respectively: maximum slip rate during the first event, mean yield stress during first event, timing of first event, mean total pressure during first event, mean fluid pressure during first event, mean effective pressure during first event.

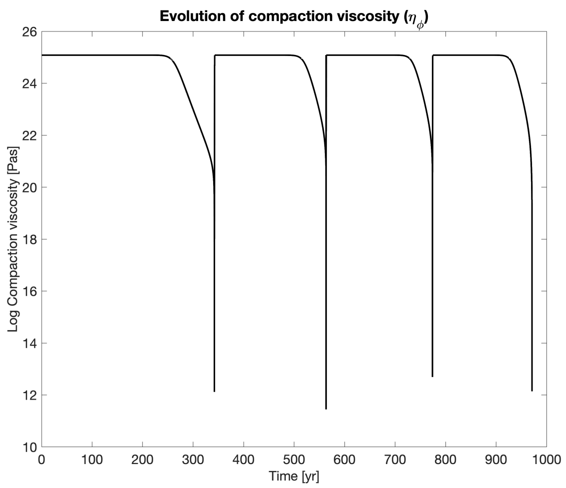

Figure 10 Evolution of the effective visco-plastic compaction viscosity through time, in the middle of the fault zone.

ing relationships for respectively permeability and compaction viscosity:

$$k_0 \sim \left(\frac{dy}{w}\right)^{n_1} \tag{21}$$

$$\eta^\phi \sim \left(\frac{dy}{w}\right)^{n_2} \tag{22}$$

where k_0 is the reference permeability, dy is the grid step size in the y direction, w is the assumed fault width (Table 1), and $n_1 = 2$ and $n_2 = 1$ are scaling exponents. The fault width is implemented as a physical parameter: it is smaller or equal to the resolution and is of the magnitude of the width of natural fault damage zones. For simplicity, during model runs, the fault width does not change with time.

Additionally, the porosity dependent permeability is:

$$k = k_0 \left(\frac{\phi}{\phi_0}\right)^{n} \tag{23}$$

where k is permeability (plotted on Fig. 5), k_0 is the reference permeability (Eq. 21), ϕ is the porosity, ϕ_0 is the reference porosity (plotted on Fig. 5), and n exponent can vary between 1 to 50 (Yarushina et al., 2013). Here $n = 3$, based on pore geometry and previous studies (Connolly and Podladchikov, 2000; Dymkova and Gerya, 2013; Morency et al., 2007; Rice, 1992).

We evaluate several parameters (maximum slip rate, mean yield stress, pressures, and timing of the first event) during the initial events of the model runs (Fig. 9). This evaluation helps us compare models across six different resolutions ranging from $dy = 450\,\text{m}$ to $dy = 1500\,\text{m}$ to investigate the convergence of the parameters with and without the scaling laws. The models without the permeability scaling law (Fig. 9, blue markers) show different seismic slip behavior as the resolution changes. For the higher resolution cases ($dy =$

$450\,\mathrm{m}, 500\,\mathrm{m}, 750\,\mathrm{m}$), the models show seismic slip behavior, and the mean pressures show only $< 5\%$ difference between the results, while the mean yield stress shows $< 10\%$ difference. However, at lower resolutions ($dy = 1000\,\mathrm{m}, 1250\,\mathrm{m}, 1500\,\mathrm{m}$), no seismicity can be observed in the models.

By using the implemented permeability scaling law, all models demonstrate similar seismic slip behavior (Fig. 9). The mean pressures and mean yield stress show approximately 5% difference between the model results after the first event. Although the maximum slip rates are more scattered, these values still fit well within the seismic slip rates of natural events (Di Toro et al., 2011). The timing of the first event increases with increased resolution, with approximately 500 years (20%) difference between the models with the highest and lowest resolutions. This implies that using the described scaling approach allows us to achieve the convergence of the model parameters and maintain the same seismic slip mode across a wide range of resolutions. While at high resolutions the model results are similar with or without the scaling law, at lower resolutions the models show different seismic behaviors without the scaling due to the high dependence of the numerical solution on the resolution. The use of the simple scaling approach provides a robust solution to make the model results nearly independent of grid step size.

B Evolution of the visco-plastic compaction viscosity

Here we provide a plot (Figure 10) that describes the evolution of the effective visco-plastic compaction viscosity (η^{ϕ}) through multiple seismic cycles. This shows the reduction in η^{ϕ} during yielding, which promotes visco-plastic compaction.

Acknowledgements

This research was funded by an ERC starting grant to Whitney M. Behr (S-SIM, Grant Number 947659). L. Dal Zilio was supported by the Earth Observatory of Singapore (EOS) and the Singapore Ministry of Education Tier 3b project “Investigating Volcano and Earthquake Science and Technology (InVEST)” (Award No. MOE-MOET32021-0002). The numerical simulations were performed on the ETH cluster Euler. The authors thank Eric Dunham and an anonymous reviewer for their valuable comments and insights that improved the manuscript. We are grateful to Seismica editor Pathikrit Bhattacharya for his work handling the manuscript and the review process.

Data and code availability

We provide the code used to perform the numerical experiments, as well as a table with the list of models used in the manuscript, in a repository (Hegyi et al., 2025).

Competing interests

The authors declare that they have no competing interests.

References

Aben, F. M. and Brantut, N. Dilatancy stabilises shear failure in rock. *Earth and Planetary Science Letters*, 574:117174, Nov. 2021. doi: 10.1016/j.epsl.2021.117174.

Abercrombie, R. E. and Rice, J. R. Can observations of earthquake scaling constrain slip weakening? *Geophysical Journal International*, 162(2):406–424, Aug. 2005. doi: 10.1111/j.1365-246x.2005.02579.x.

Alghannam, M. and Juanes, R. Understanding rate effects in injection-induced earthquakes. *Nature Communications*, 11(1), 2020. doi: 10.1038/s41467-020-16860-y.

Allmann, B. P. and Shearer, P. M. Global variations of stress drop for moderate to large earthquakes. *Journal of Geophysical Research: Solid Earth*, 114(B1), Jan. 2009. doi: 10.1029/2008jb005821.

Angiboust, S., Kirsch, J., Oncken, O., Glodny, J., Monié, P., and Rybacki, E. Probing the transition between seismically coupled and decoupled segments along an ancient subduction interface. *Geochemistry, Geophysics, Geosystems*, 16(6), 2015. doi: 10.1002/2015gc005776.

Aretusini, S., Meneghini, F., Spagnuolo, E., Harbord, C. W., and Di Toro, G. Fluid pressurisation and earthquake propagation in the Hikurangi subduction zone. *Nature Communications*, 12(1), Apr. 2021. doi: 10.1038/s41467-021-22805-w.

Ashman, I. R. and Faulkner, D. R. The Effect of Clay Content on the Dilatancy and Frictional Properties of Fault Gouge. *Journal of Geophysical Research: Solid Earth*, 128(4), Apr. 2023. doi: 10.1029/2022jb025878.

Audet, P. and Bürgmann, R. Possible control of subduction zone slow-earthquake periodicity by silica enrichment. *Nature*, 510 (7505), 2014. doi: 10.1038/nature13391.

Barbot, S., Lapusta, N., and Avouac, J.-P. Under the Hood of the Earthquake Machine: Toward Predictive Modeling of the Seismic Cycle. *Science*, 336(6082):707–710, May 2012. doi: 10.1126/science.1218796.

Beeler, N. M., Thomas, A., Bürgmann, R., and Shelly, D. Constraints on Friction, Dilatancy, Diffusivity, and Effective Stress From Low-Frequency Earthquake Rates on the Deep San Andreas Fault. *Journal of Geophysical Research: Solid Earth*, 123 (1):583–605, Jan. 2018. doi: 10.1002/2017jb015052.

Behr, W. and Bürgmann, R. What's down there? The structures, materials and environment of deep-seated slow slip and tremor. preprint, 2020. doi: 10.31223/osf.io/tyzb9.

Behr, W. M., Gerya, T. V., Cannizzaro, C., and Blass, R. Transient Slow Slip Characteristics of Frictional-Viscous Subduction Megathrust Shear Zones. *AGU Advances*, 2(3), 2021. doi: 10.1029/2021av000416.

Brace, W. F., Paulding, B. W., and Scholz, C. Dilatancy in the fracture of crystalline rocks. *Journal of Geophysical Research*, 71 (16):3939–3953, Aug. 1966. doi: 10.1029/jz071i016p03939.

Brantut, N. Dilatancy-induced fluid pressure drop during dynamic rupture: Direct experimental evidence and consequences for earthquake dynamics. *Earth and Planetary Science Letters*, 538: 116179, May 2020. doi: 10.1016/j.epsl.2020.116179.

Brantut, N. Dilatancy Toughening of Shear Cracks and Implications for Slow Rupture Propagation. *Journal of Geophysical Research: Solid Earth*, 126(11), Nov. 2021. doi: 10.1029/2021jb022239.

Brantut, N., Baker, M., Hansen, L. N., and Baud, P. Microstructural Control of Physical Properties During Deformation of Porous Limestone. *Journal of Geophysical Research: Solid Earth*, 123 (6), 2018. doi: 10.1029/2018jb015636.

Bürgmann, R. The geophysics, geology and mechanics of slow fault slip. *Earth and Planetary Science Letters*, 495:112–134, Aug. 2018. doi: 10.1016/j.epsl.2018.04.062.

Caniven, Y., Morgan, J. K., and Blank, D. G. The Role of Along-Fault Dilatancy in Fault Slip Behavior. *Journal of Geophysical Research: Solid Earth*, 126(11), Nov. 2021. doi: 10.1029/2021jb022310.

Cappa, F. Influence of hydromechanical heterogeneities of fault zones on earthquake ruptures. *Geophysical Journal International*, 185(2):1049–1058, Mar. 2011. doi: 10.1111/j.1365-246x.2011.04994.x.

Chen, J. and Niemeijer, A. R. Seismogenic Potential of a Gouge-filled Fault and the Criterion for Its Slip Stability: Constraints From a Microphysical Model. *Journal of Geophysical Research: Solid Earth*, 122(12):9658–9688, Dec. 2017. doi: 10.1002/2017jb014228.

Chen, T. and Lapusta, N. Scaling of small repeating earthquakes explained by interaction of seismic and aseismic slip in a rate and state fault model. *Journal of Geophysical Research: Solid Earth*, 114(B1), Jan. 2009. doi: 10.1029/2008jb005749.

Ciardo, F. and Lecampion, B. Effect of Dilatancy on the Transition From Aseismic to Seismic Slip Due to Fluid Injection in a Fault. *Journal of Geophysical Research: Solid Earth*, 124(4):3724–3743, Apr. 2019. doi: 10.1029/2018jb016636.

Condit, C. B. and French, M. E. Geologic Evidence of Lithostatic Pore Fluid Pressures at the Base of the Subduction Seismogenic Zone. *Geophysical Research Letters*, 49(12), 2022. doi: 10.1029/2022gl098862.

Connolly, J. and Podladchikov, Y. Temperature-dependent viscoelastic compaction and compartmentalization in sedimentary basins. *Tectonophysics*, 324(3), 2000. doi: 10.1016/s0040-1951(00)00084-6.

Cox, S. F. *Coupling between Deformation, Fluid Pressures, and Fluid Flow in Ore-Producing Hydrothermal Systems at Depth in the Crust*. Society of Economic Geologists, 2005. doi: 10.5382/av100.04.

Dal Zilio, L. and Gerya, T. Subduction earthquake cycles controlled by episodic fluid pressure cycling. *Lithos*, 426-427:106800, Oct. 2022. doi: 10.1016/j.lithos.2022.106800.

Dal Zilio, L., Lapusta, N., and Avouac, J. Unraveling Scaling Properties of Slow-Slip Events. *Geophysical Research Letters*, 47(10), May 2020. doi: 10.1029/2020gl087477.

Dal Zilio, L., Hegyi, B., Behr, W., and Gerya, T. Hydro-mechanical earthquake cycles in a poro-visco-elasto-plastic fluid-bearing fault structure. *Tectonophysics*, 838, 2022. doi: 10.1016/j.tecto.2022.229516.

Day, S. M., Dalguer, L. A., Lapusta, N., and Liu, Y. Comparison of finite difference and boundary integral solutions to three-dimensional spontaneous rupture. *Journal of Geophysical Research: Solid Earth*, 110(B12), Dec. 2005. doi: 10.1029/2005jb003813.

Di Toro, G., Han, R., Hirose, T., De Paola, N., Nielsen, S., Mizoguchi, K., Ferri, F., Cocco, M., and Shimamoto, T. Fault lubrication during earthquakes. *Nature*, 471(7339):494–498, Mar. 2011. doi: 10.1038/nature09838.

Dieterich, J. H. Time-Dependent Friction and the Mechanics of Stick-Slip. *Pure and Applied Geophysics*, 116, 1978. doi: 10.1007/BF00876539.

Drucker, D. C. and Prager, W. Soil mechanics and plastic analysis or limit design. *Quarterly of Applied Mathematics*, 10(2), 1952. doi: 10.1090/qam/48291.

Dymkova, D. and Gerya, T. Porous fluid flow enables oceanic subduction initiation on Earth. *Geophysical Research Letters*, 40 (21):5671–5676, Nov. 2013. doi: 10.1002/2013gl057798.

Ellsworth, W. L. Injection-Induced Earthquakes. *Science*, 341 (6142), 2013. doi: 10.1126/science.1225942.

Erickson, B. A. and Day, S. M. Bimaterial effects in an earthquake cycle model using rate-and-state friction. *Journal of Geophysical Research: Solid Earth*, 121(4):2480–2506, Apr. 2016. doi: 10.1002/2015jb012470.

Fagereng, A., Diener, J. F., Meneghini, F., Harris, C., and Kvadsheim, A. Quartz vein formation by local dehydration embrittlement along the deep, tremorgenic subduction thrust interface. *Geology*, 46(1):67–70, Nov. 2017. doi: 10.1130/g39649.1.

Farge, G., Jaupart, C., and Shapiro, N. M. Episodicity and Migration of Low Frequency Earthquakes Modeled With Fast Fluid Pressure Transients in the Permeable Subduction Interface. *Journal of Geophysical Research: Solid Earth*, 126(9), 2021. doi: 10.1029/2021jb021894.

Faulkner, D., Jackson, C., Lunn, R., Schlische, R., Shipton, Z., Wibberley, C., and Withjack, M. A review of recent developments concerning the structure, mechanics and fluid flow properties of fault zones. *Journal of Structural Geology*, 32(11):1557–1575, Nov. 2010. doi: 10.1016/j.jsg.2010.06.009.

Frank, W., Shapiro, N., Husker, A., Kostoglodov, V., Bhat, H., and Campillo, M. Along-fault pore-pressure evolution during a slow-slip event in Guerrero, Mexico. *Earth and Planetary Science Letters*, 413:135–143, Mar. 2015. doi: 10.1016/j.epsl.2014.12.051.

Gerya, T. *Introduction to Numerical Geodynamic Modelling*. Cambridge University Press, May 2019. doi: 10.1017/9781316534243.

Goldsby, D. L. and Tullis, T. E. Flash Heating Leads to Low Frictional Strength of Crustal Rocks at Earthquake Slip Rates. *Science*, 334 (6053):216–218, Oct. 2011. doi: 10.1126/science.1207902.

Goren, L., Aharonov, E., Sparks, D., and Toussaint, R. Pore pressure evolution in deforming granular material: A general formulation and the infinitely stiff approximation. *Journal of Geophysical Research: Solid Earth*, 115(B9), 2010. doi: 10.1029/2009jb007191.

Hainzl, S. Seismicity patterns of earthquake swarms due to fluid intrusion and stress triggering. *Geophysical Journal International*, 159(3):1090–1096, Dec. 2004. doi: 10.1111/j.1365-246x.2004.02463.x.

Hegyi, B., Dal Zilio, L., Behr, W. M., and Gerya, T. Dataset for "Modeling fluid-driven fault slip dynamics with shear-induced dilation and compaction", 2025. doi: 10.3929/ETHZ-B-000744898.

Heimisson, E. R., Dunham, E. M., and Almquist, M. Poroelastic effects destabilize mildly rate-strengthening friction to generate stable slow slip pulses. *Journal of the Mechanics and Physics of Solids*, 130, 2019. doi: 10.1016/j.jmps.2019.06.007.

Herrendörfer, R., Gerya, T., and van Dinther, Y. An Invariant Rate-and State-Dependent Friction Formulation for Viscoeastoplastic Earthquake Cycle Simulations. *Journal of Geophysical Research: Solid Earth*, 123(6), 2018. doi: 10.1029/2017jb015225.

Ide, S. Striations, duration, migration and tidal response in deep tremor. *Nature*, 466(7304), 2010. doi: 10.1038/nature09251.

Iverson, R. M. Regulation of landslide motion by dilatancy and pore pressure feedback. *Journal of Geophysical Research: Earth Surface*, 110(F2), 2005. doi: 10.1029/2004jf000268.

Jiang, J., Erickson, B. A., Lambert, V. R., Ampuero, J.-P., Ando, R., Barbot, S. D., Cattania, C., Zilio, L. D., Duan, B., Dunham, E. M., et al. Community-driven code comparisons for three-dimensional dynamic modeling of sequences of earthquakes and aseismic slip. *Journal of Geophysical Research: Solid Earth*, 127(3):e2021JB023519, 2022. doi: 10.1029/2021JB023519.

Lambert, V., Lapusta, N., and Perry, S. Propagation of large earthquakes as self-healing pulses or mild cracks. *Nature*, 591(7849): 252–258, Mar. 2021. doi: 10.1038/s41586-021-03248-1.

Lapusta, N., Rice, J. R., Ben-Zion, Y., and Zheng, G. Elastodynamic analysis for slow tectonic loading with spontaneous rupture episodes on faults with rate- and state-dependent friction. *Journal of Geophysical Research: Solid Earth*, 105(B10): 23765–23789, Oct. 2000. doi: 10.1029/2000jb900250.

Liu, Y. and Rice, J. R. Spontaneous and triggered aseismic deformation transients in a subduction fault model. *Journal of Geophysical Research: Solid Earth*, 112(B9), 2007. doi: 10.1029/2007jb004930.

Lockner, D. A. and Byerlee, J. D. Dilatancy in hydraulically isolated faults and the suppression of instability. *Geophysical Research Letters*, 21(22):2353–2356, Nov. 1994. doi: 10.1029/94gl02366.

Marguin, V. and Simpson, G. Influence of Fluids on Earthquakes Based on Numerical Modeling. *Journal of Geophysical Research: Solid Earth*, 128(2), Feb. 2023. doi: 10.1029/2022jb025132.

Marone, C. LABORATORY-DERIVED FRICTION LAWS AND THEIR APPLICATION TO SEISMIC FAULTING. *Annual Review of Earth and Planetary Sciences*, 26(1):643–696, May 1998. doi: 10.1146/annurev.earth.26.1.643.

Marone, C., Raleigh, C. B., and Scholz, C. H. Frictional behavior and constitutive modeling of simulated fault gouge. *Journal of Geophysical Research: Solid Earth*, 95(B5):7007–7025, May 1990. doi: 10.1029/jb095ib05p07007.

Miller, S. A. *The Role of Fluids in Tectonic and Earthquake Processes*, page 1–46. Elsevier, 2013. doi: 10.1016/b978-0-12-380940-7.00001-9.

Miller, S. A. Aftershocks are fluid-driven and decay rates controlled by permeability dynamics. *Nature Communications*, 11(1), Nov. 2020. doi: 10.1038/s41467-020-19590-3.

Miller, S. A., Collettini, C., Chiaraluce, L., Cocco, M., Barchi, M., and Kaus, B. J. P. Aftershocks driven by a high-pressure CO2 source at depth. *Nature*, 427(6976):724–727, Feb. 2004. doi: 10.1038/nature02251.

Morency, C., Huismans, R. S., Beaumont, C., and Fullsack, P. A numerical model for coupled fluid flow and matrix deformation with applications to disequilibrium compaction and delta stability. *Journal of Geophysical Research: Solid Earth*, 112(B10), Oct. 2007. doi: 10.1029/2006jb004701.

Muñoz-Montecinos, J., Angiboust, S., Garcia-Casco, A., Glodny, J., and Bebout, G. Episodic hydrofracturing and large-scale flushing along deep subduction interfaces: Implications for fluid transfer and carbon recycling (Zagros Orogen, southeastern Iran). *Chemical Geology*, 571, 2021. doi: 10.1016/j.chemgeo.2021.120173.

Muñoz-Montecinos, J. and Behr, W. M. Transient Permeability of a Deep-Seated Subduction Interface Shear Zone. *Geophysical Research Letters*, 50(20), Oct. 2023. doi: 10.1029/2023gl104244.

Niemeijer, A. R. and Spiers, C. J. A microphysical model for strong velocity weakening in phyllosilicate-bearing fault gouges. *Journal of Geophysical Research: Solid Earth*, 112(B10), Oct. 2007. doi: 10.1029/2007jb005008.

Noda, H. and Lapusta, N. Stable creeping fault segments can become destructive as a result of dynamic weakening. *Nature*, 493 (7433):518–521, Jan. 2013. doi: 10.1038/nature11703.

Noda, H., Dunham, E. M., and Rice, J. R. Earthquake ruptures with thermal weakening and the operation of major faults at low overall stress levels. *Journal of Geophysical Research: Solid Earth*, 114(B7), 2009. doi: 10.1029/2008jb006143.

Nur, A. Dilatancy, pore fluids, and premonitory variations of ts/tp travel times. *Bulletin of the Seismological Society of America*, 62 (5):1217–1222, Oct. 1972. doi: 10.1785/bssa0620051217.

Parez, S., Kozakovic, M., and Havlica, J. Pore Pressure Drop During Dynamic Rupture and Conditions for Dilatancy Hardening. *Journal of Geophysical Research: Solid Earth*, 128(7), 2023. doi: 10.1029/2023jb026396.

Peacock, S. M., Christensen, N. I., Bostock, M. G., and Audet, P. High pore pressures and porosity at 35 km depth in the Cascadia subduction zone. *Geology*, 39(5):471–474, Mar. 2011. doi: 10.1130/g31649.1.

Petrini, C., Gerya, T., Yarushina, V., van Dinther, Y., Connolly, J., and Madonna, C. Seismo-hydro-mechanical modelling of the seismic cycle: Methodology and implications for subduction zone seismicity. *Tectonophysics*, 791, 2020. doi: 10.1016/j.tecto.2020.228504.

Proctor, B., Lockner, D. A., Kilgore, B. D., Mitchell, T. M., and Beeler, N. M. Direct Evidence for Fluid Pressure, Dilatancy, and Compaction Affecting Slip in Isolated Faults. *Geophysical Research Letters*, 47(16), Aug. 2020. doi: 10.1029/2019gl086767.

Rice, J. R. *Fault stress states, pore pressure distributions, and the weakness of the San Andreas fault*, page 475–503. Elsevier, 1992. doi: 10.1016/s0074-6142(08)62835-1.

Rice, J. R. Heating and weakening of faults during earthquake slip. *Journal of Geophysical Research: Solid Earth*, 111(B5), May 2006. doi: 10.1029/2005jb004006.

Rice, J. R. and Rudnicki, J. W. Earthquake precursory effects due to pore fluid stabilization of a weakening fault zone. *Journal of Geophysical Research: Solid Earth*, 84(B5):2177–2193, May 1979. doi: 10.1029/jb084ib05p02177.

Ross, Z. E., Cochran, E. S., Trugman, D. T., and Smith, J. D. 3D fault architecture controls the dynamism of earthquake swarms. *Science*, 368(6497), 2020. doi: 10.1126/science.abb0779.

Rudnicki, J. W. and Chen, C. Stabilization of rapid frictional slip on a weakening fault by dilatant hardening. *Journal of Geophysical Research: Solid Earth*, 93(B5):4745–4757, May 1988. doi: 10.1029/jb093ib05p04745.

Ruina, A. Slip instability and state variable friction laws. *Journal of Geophysical Research: Solid Earth*, 88(B12):10359–10370, Dec. 1983. doi: 10.1029/jb088ib12p10359.

Rutqvist, J. Fractured rock stress–permeability relationships from in situ data and effects of temperature and chemical–mechanical couplings, Jan. 2012. doi: 10.1002/9781119166573.ch8.

Samuelson, J., Elsworth, D., and Marone, C. Shear-induced dilatancy of fluid-saturated faults: Experiment and theory. *Journal of Geophysical Research: Solid Earth*, 114(B12), Dec. 2009. doi: 10.1029/2008jb006273.

Sarma, P., Aharonov, E., Toussaint, R., and Parez, S. Fault Gouge Failure Induced by Fluid Injection: Hysteresis, Delay and Shear-Strengthening. *Journal of Geophysical Research: Solid Earth*, 130(6), 2025. doi: 10.1029/2024jb030768.

Scholz, C. H. Earthquakes and friction laws. *Nature*, 391(6662): 37–42, Jan. 1998. doi: 10.1038/34097.

Segall, P. and Rice, J. R. Dilatancy, compaction, and slip instability of a fluid-infiltrated fault. *Journal of Geophysical Research: Solid Earth*, 100(B11):22155–22171, Nov. 1995. doi: 10.1029/95jb02403.

Segall, P., Rubin, A. M., Bradley, A. M., and Rice, J. R. Dilatant strengthening as a mechanism for slow slip events. *Journal of Geophysical Research: Solid Earth*, 115(B12), Dec. 2010. doi: 10.1029/2010jb007449.

Shelly, D. R. and Hill, D. P. Migrating swarms of brittle-failure earthquakes in the lower crust beneath Mammoth Mountain, California. *Geophysical Research Letters*, 38(20), Oct. 2011. doi: 10.1029/2011gl049336.

Shimamoto, T. and Noda, H. A friction to flow constitutive law and its application to a 2-D modeling of earthquakes. *Journal of Geophysical Research: Solid Earth*, 119(11):8089–8106, Nov. 2014. doi: 10.1002/2014jb011170.

Sibson, R. Implications of fault-valve behaviour for rupture nucleation and recurrence. *Tectonophysics*, 211(1-4), 1992a. doi: 10.1016/0040-1951(92)90065-e.

Sibson, R. H. Stopping of earthquake ruptures at dilational fault jogs. *Nature*, 316(6025), 1985. doi: 10.1038/316248a0.

Sibson, R. H. Brecciation processes in fault zones: Inferences from earthquake rupturing. *pure and applied geophysics*, 124(1-2): 159–175, Jan. 1986. doi: 10.1007/bf00875724.

Sibson, R. H. Rupture nucleation on unfavorably oriented faults. *Bulletin of the Seismological Society of America*, 80(6A): 1580–1604, 1990.

Sibson, R. H. Fault-valve behavior and the hydrostatic-lithostatic fluid pressure interface. *Earth-Science Reviews*, 32(1-2): 141–144, Jan. 1992b. doi: 10.1016/0012-8252(92)90019-p.

Sibson, R. H. Tensile overpressure compartments on low-angle thrust faults. *Earth, Planets and Space*, 69(1), Aug. 2017. doi: 10.1186/s40623-017-0699-y.

Stanton-Yonge, A., Sánchez De La Muela, A., Pearce, R. K., Hammond, J. O., Mitchell, T. M., Hicks, S. P., Griffith, W. A., Moorkamp, M., Meredith, P. G., and Cembrano, J. Fluid pressure fluctuations and the seismic signature of a fault-controlled fluid migration pulse. *Earth and Planetary Science Letters*, 662, 2025. doi: 10.1016/j.epsl.2025.119388.

Tewksbury-Christle, C. M. and Behr, W. M. Constraints From Exhumed Rocks on the Seismic Signature of the Deep Subduction Interface. *Geophysical Research Letters*, 48(18), 2021. doi: 10.1029/2021gl093831.

Tsutsumi, A. and Shimamoto, T. High-velocity frictional properties of gabbro. *Geophysical Research Letters*, 24(6):699–702, Mar. 1997. doi: 10.1029/97gl00503.

van den Ende, M., Chen, J., Ampuero, J.-P., and Niemeijer, A. A comparison between rate-and-state friction and microphysical models, based on numerical simulations of fault slip. *Tectonophysics*, 733:273–295, May 2018. doi: 10.1016/j.tecto.2017.11.040.

Viesca, R. C. and Garagash, D. I. Ubiquitous weakening of faults due to thermal pressurization. *Nature Geoscience*, 8(11):875–879, Oct. 2015. doi: 10.1038/ngeo2554.

Woodcock, N. H., Dickson, J. A. D., and Tarasewicz, J. P. T. Transient permeability and reseal hardening in fault zones: evidence from dilation breccia textures. *Geological Society, London, Special Publications*, 270(1):43–53, Jan. 2007. doi: 10.1144/gsl.sp.2007.270.01.03.

Xing, T., Zhu, W., French, M., and Belzer, B. Stabilizing Effect of High Pore Fluid Pressure on Slip Behaviors of Gouge-bearing Faults. *Journal of Geophysical Research: Solid Earth*, 124(9), 2019. doi: 10.1029/2019jb018002.

Yang, Y. and Dunham, E. M. Effect of porosity and permeability evolution on injection-induced aseismic slip. *Journal of Geophysical Research: Solid Earth*, 126(7):e2020JB021258, 2021. doi: 10.1029/2020JB021258.

Yarushina, V. M. and Podladchikov, Y. Y. (De)compaction of porous viscoelastoplastic media: Model formulation. *Journal of Geophysical Research: Solid Earth*, 120(6), 2015. doi: 10.1002/2014jb011258.

Yarushina, V. M., Bercovici, D., and Oristaglio, M. L. Rock deformation models and fluid leak-off in hydraulic fracturing. *Geophysical Journal International*, 194(3), 2013. doi: 10.1093/gji/ggt199.

Yarushina, V. M., Podladchikov, Y. Y., and Connolly, J. A. D. (De)compaction of porous viscoelastoplastic media: Solitary porosity waves. *Journal of Geophysical Research: Solid Earth*, 120(7), 2015. doi: 10.1002/2014jb011260.

Yi, J. T., Li, Y. P., Bai, S., Fu, Y., Lee, F. H., and Zhang, X. Y. A Simple Effective Stress Approach for Modeling Rate-Dependent Strength of Soft Clay. *Journal of Offshore Mechanics and Arctic Engineering*, 140(4), Jan. 2018. doi: 10.1115/1.4038732.

Zhao, X. and Cai, M. A mobilized dilation angle model for rocks. *International Journal of Rock Mechanics and Mining Sciences*, 47 (3):368–384, Apr. 2010. doi: 10.1016/j.ijrmms.2009.12.007.

Zhu, W., Allison, K. L., Dunham, E. M., and Yang, Y. Fault valving and pore pressure evolution in simulations of earthquake sequences and aseismic slip. *Nature Communications*, 11(1), 2020. doi: 10.1038/s41467-020-18598-z.